

Syracuse University

SURFACE

Physics

College of Arts and Sciences

4-15-2011

Beating the Spin-Down Limit on Gravitational Wave Emission from the Vela Pulsar

Duncan Brown

Department of Physics, Syracuse University, Syracuse, NY

J. Abadie

California Institute of Technology

Collin Capano

Syracuse University

J. A. Garofoli

Syracuse University

A. P. Lundgren

Syracuse University

Follow this and additional works at: <https://surface.syr.edu/phy>



Part of the [Physics Commons](#)

Recommended Citation

Brown, Duncan; Abadie, J.; Capano, Collin; Garofoli, J. A.; and Lundgren, A. P., "Beating the Spin-Down Limit on Gravitational Wave Emission from the Vela Pulsar" (2011). *Physics*. 237.

<https://surface.syr.edu/phy/237>

This Article is brought to you for free and open access by the College of Arts and Sciences at SURFACE. It has been accepted for inclusion in Physics by an authorized administrator of SURFACE. For more information, please contact surface@syr.edu.

Beating the spin-down limit on gravitational wave emission from the Vela pulsar

J. Abadie¹, B. P. Abbott¹, R. Abbott¹, M. Abernathy², T. Accadia³, F. Acernese^{4ac}, C. Adams⁵, R. Adhikari¹, C. Affeldt^{6,7}, B. Allen^{6,8,7}, G. S. Allen⁹, E. Amador Ceron⁸, D. Amariutei¹⁰, R. S. Amin¹¹, S. B. Anderson¹, W. G. Anderson⁸, F. Antonucci^{12a}, K. Arai¹, M. A. Arain¹⁰, M. C. Araya¹, S. M. Aston¹³, P. Astone^{12a}, D. Atkinson¹⁴, P. Aufmuth^{7,6}, C. Aulbert^{6,7}, B. E. Aylott¹³, S. Babak¹⁵, P. Baker¹⁶, G. Ballardín¹⁷, S. Ballmer¹, D. Barker¹⁴, S. Barnum¹⁸, F. Barone^{4ac}, B. Barr², P. Barriga¹⁹, L. Barsotti²⁰, M. Barsuglia²¹, M. A. Barton¹⁴, I. Bartos²², R. Bassiri², M. Bastarrika², A. Basti^{23ab}, J. Bauchrowitz^{6,7}, Th. S. Bauer^{24a}, B. Behnke¹⁵, M. Bejger^{38c}, M.G. Beker^{24a}, A. S. Bell², A. Belletoile³, I. Belopolski²², M. Benacquista²⁵, A. Bertolini^{6,7}, J. Betzwieser¹, N. Beveridge², P. T. Beyersdorf²⁶, I. A. Bilenko²⁷, G. Billingsley¹, J. Birch⁵, S. Birindelli^{28a}, R. Biswas⁸, M. Bitossi^{23a}, M. A. Bizouard^{29a}, E. Black¹, J. K. Blackburn¹, L. Blackburn²⁰, D. Blair¹⁹, B. Bland¹⁴, M. Blom^{24a}, O. Bock^{6,7}, T. P. Bodiya²⁰, C. Bogan^{6,7}, R. Bondarescu³⁰, F. Bondu^{28b}, L. Bonelli^{23ab}, R. Bonnard³¹, R. Bork¹, M. Born^{6,7}, V. Boschi^{23a}, S. Bose³², L. Bosi^{33a}, B. Bouhou²¹, M. Boyle³⁴, S. Braccini^{23a}, C. Bradaschia^{23a}, P. R. Brady⁸, V. B. Braginsky²⁷, J. E. Brau³⁵, J. Breyer^{6,7}, D. O. Bridges⁵, A. Brillet^{28a}, M. Brinkmann^{6,7}, V. Brisson^{29a}, M. Britzger^{6,7}, A. F. Brooks¹, D. A. Brown³⁶, A. Brummit³⁷, R. Budzyński^{38b}, T. Bulik^{38bc}, H. J. Bulten^{24ab}, A. Buonanno³⁹, J. Burguet-Castell⁸, O. Burmeister^{6,7}, D. Buskulic³, C. Buy²¹, R. L. Byer⁹, L. Cadonati⁴⁰, G. Cagnoli^{41a}, J. Cain⁴², E. Calloni^{4ab}, J. B. Camp⁴³, E. Campagna^{41ab}, P. Campsie², J. Cannizzo⁴³, K. Cannon¹, B. Canuel¹⁷, J. Cao⁴⁴, C. Capano³⁶, F. Carbognani¹⁷, S. Caride⁴⁵, S. Caudill¹¹, M. Cavaglia⁴², F. Cavalier^{29a}, R. Cavalieri¹⁷, G. Cella^{23a}, C. Cepeda¹, E. Cesarini^{41b}, O. Chaibi^{28a}, T. Chalermongsak¹, E. Chalkley¹³, P. Charlton⁴⁶, E. Chassande-Mottin²¹, S. Chelkowski¹³, Y. Chen³⁴, A. Chincarini⁴⁷, N. Christensen¹⁸, S. S. Y. Chua⁴⁸, C. T. Y. Chung⁴⁹, S. Chung¹⁹, F. Clara¹⁴, D. Clark⁹, J. Clark⁵⁰, J. H. Clayton⁸, F. Cleva^{28a}, E. Coccia^{51ab}, C. N. Colacino^{23ab}, J. Colas¹⁷, A. Colla^{12ab}, M. Colombini^{12b}, R. Conte⁵², D. Cook¹⁴, T. R. Corbitt²⁰, N. Cornish¹⁶, A. Corsi^{12a}, C. A. Costa¹¹, M. Coughlin¹⁸, J.-P. Coulon^{28a}, D. M. Coward¹⁹, D. C. Coyne¹, J. D. E. Creighton⁸, T. D. Creighton²⁵, A. M. Cruise¹³, R. M. Culter¹³, A. Cumming², L. Cunningham², E. Cuoco¹⁷, K. Dahl^{6,7}, S. L. Danilishin²⁷, R. Dannenberg¹, S. D'Antonio^{51a}, K. Danzmann^{6,7}, K. Das¹⁰, V. Dattilo¹⁷, B. Daudert¹, H. Daveloza²⁵, M. Davier^{29a}, G. Davies⁵⁰, E. J. Daw⁵³, R. Day¹⁷, T. Dayanga³², R. De Rosa^{4ab}, D. DeBra⁹, G. Debreczeni⁵⁴, J. Degallaix^{6,7}, M. del Prete^{23ac}, T. Dent⁵⁰, V. Dergachev¹, R. DeRosa¹¹, R. DeSalvo¹, S. Dhurandhar⁵⁵, L. Di Fiore^{4a}, A. Di Lieto^{23ab}, I. Di Palma^{6,7}, M. Di Paolo Emilio^{51ac}, A. Di Virgilio^{23a}, M. Díaz²⁵, A. Dietz³, F. Donovan²⁰, K. L. Dooley¹⁰, S. Dorsher⁵⁶, E. S. D. Douglas¹⁴, M. Drago^{57cd},

R. W. P. Drever⁵⁸, J. C. Driggers¹, J.-C. Dumas¹⁹, S. Dwyer²⁰, T. Eberle^{6,7}, M. Edgar², M. Edwards⁵⁰, A. Effler¹¹, P. Ehrens¹, R. Engel¹, T. Etzel¹, M. Evans²⁰, T. Evans⁵, M. Factourovich²², V. Fafone^{51ab}, S. Fairhurst⁵⁰, Y. Fan¹⁹, B. F. Farr⁵⁹, D. Fazi⁵⁹, H. Fehrmann^{6,7}, D. Feldbaum¹⁰, I. Ferrante^{23ab}, F. Fidecaro^{23ab}, L. S. Finn³⁰, I. Fiori¹⁷, R. Flaminio³¹, M. Flanigan¹⁴, S. Foley²⁰, E. Forzi⁵, L. A. Forte^{4a}, N. Fotopoulos⁸, J.-D. Fournier^{28a}, J. Franc³¹, S. Frasca^{12ab}, F. Frasconi^{23a}, M. Frede^{6,7}, M. Frei⁶⁰, Z. Frei⁶¹, A. Freise¹³, R. Frey³⁵, T. T. Fricke¹¹, D. Friedrich^{6,7}, P. Fritschel²⁰, V. V. Frolov⁵, P. Fulda¹³, M. Fyffe⁵, M. Galimberti³¹, L. Gammaitoni^{33ab}, J. Garcia¹⁴, J. A. Garofoli³⁶, F. Garufi^{4ab}, M. E. Gáspár⁵⁴, G. Gemme⁴⁷, E. Genin¹⁷, A. Gennai^{23a}, S. Ghosh³², J. A. Giaime^{11,5}, S. Giampanis^{6,7}, K. D. Giardina⁵, A. Giazotto^{23a}, C. Gill², E. Goetz⁴⁵, L. M. Goggin⁸, G. González¹¹, M. L. Gorodetsky²⁷, S. Gößler^{6,7}, R. Gouaty³, C. Graef^{6,7}, M. Granata²¹, A. Grant², S. Gras¹⁹, C. Gray¹⁴, R. J. S. Greenhalgh³⁷, A. M. Gretarsson⁶², C. Greverie^{28a}, R. Grosso²⁵, H. Grote^{6,7}, S. Grunewald¹⁵, G. M. Guidi^{41ab}, C. Guido⁵, R. Gupta⁵⁵, E. K. Gustafson¹, R. Gustafson⁴⁵, B. Hage^{7,6}, J. M. Hallam¹³, D. Hammer⁸, G. Hammond², J. Hanks¹⁴, C. Hanna¹, J. Hanson⁵, J. Harms⁵⁸, G. M. Harry²⁰, I. W. Harry⁵⁰, E. D. Harstad³⁵, M. T. Hartman¹⁰, K. Haughian², K. Hayama⁶³, J.-F. Hayau^{28b}, T. Hayler³⁷, J. Heefner¹, H. Heitmann²⁸, P. Hello^{29a}, M. A. Hendry², I. S. Heng², A. W. Heptonstall¹, V. Herrera⁹, M. Hewitson^{6,7}, S. Hild², D. Hoak⁴⁰, K. A. Hodge¹, K. Holt⁵, T. Hong³⁴, S. Hooper¹⁹, D. J. Hosken⁶⁴, J. Hough², E. J. Howell¹⁹, D. Huet¹⁷, B. Hughey²⁰, S. Husa⁶⁵, S. H. Huttner², D. R. Ingram¹⁴, R. Inta⁴⁸, T. Isogai¹⁸, A. Ivanov¹, P. Jaranowski^{38d}, W. W. Johnson¹¹, D. I. Jones⁶⁶, G. Jones⁵⁰, R. Jones², L. Ju¹⁹, P. Kalmus¹, V. Kalogera⁵⁹, S. Kandhasamy⁵⁶, J. B. Kanner³⁹, E. Katsavounidis²⁰, W. Katzman⁵, K. Kawabe¹⁴, S. Kawamura⁶³, F. Kawazoe^{6,7}, W. Kells¹, M. Kelner⁵⁹, D. G. Keppel¹, A. Khalaidovski^{6,7}, F. Y. Khalili²⁷, E. A. Khazanov⁶⁷, H. Kim^{6,7}, N. Kim⁹, P. J. King¹, D. L. Kinzel⁵, J. S. Kissel¹¹, S. Klimenko¹⁰, V. Kondrashov¹, R. Kopparapu³⁰, S. Koranda⁸, W. Z. Korth¹, I. Kowalska^{38b}, D. Kozak¹, V. Kringel^{6,7}, S. Krishnamurthy⁵⁹, B. Krishnan¹⁵, A. Królak^{38ae}, G. Kuehn^{6,7}, R. Kumar², P. Kwee^{7,6}, M. Landry¹⁴, B. Lantz⁹, N. Lastzka^{6,7}, A. Lazzarini¹, P. Leaci¹⁵, J. Leong^{6,7}, I. Leonor³⁵, N. Leroy^{29a}, N. Letendre³, J. Li²⁵, T. G. F. Li^{24a}, N. Liguori^{57ab}, P. E. Lindquist¹, N. A. Lockerbie⁶⁸, D. Lodhia¹³, M. Lorenzini^{41a}, V. Loriette^{29b}, M. Lormand⁵, G. Losurdo^{41a}, P. Lu⁹, J. Luan³⁴, M. Lubinski¹⁴, H. Lück^{6,7}, A. P. Lundgren³⁶, E. Macdonald², B. Machenschalk^{6,7}, M. MacInnis²⁰, M. Mageswaran¹, K. Mailand¹, E. Majorana^{12a}, I. Maksimovic^{29b}, N. Man^{28a}, I. Mandel⁵⁹, V. Mandic⁵⁶, M. Mantovani^{23ac}, A. Marandi⁹, F. Marchesoni^{33a}, F. Marion³, S. Márka²², Z. Márka²², E. Maros¹, J. Marque¹⁷, F. Martelli^{41ab}, I. W. Martin², R. M. Martin¹⁰, J. N. Marx¹, K. Mason²⁰, A. Masserot³, F. Matichard²⁰, L. Matone²², R. A. Matzner⁶⁰, N. Mavalvala²⁰, R. McCarthy¹⁴, D. E. McClelland⁴⁸, S. C. McGuire⁶⁹, G. McIntyre¹, D. J. A. McKechnan⁵⁰, G. Meadors⁴⁵, M. Mehmet^{6,7}, T. Meier^{7,6}, A. Melatos⁴⁹, A. C. Melissinos⁷⁰, G. Mendell¹⁴, R. A. Mercer⁸, L. Merrill¹⁹, S. Meshkov¹,

C. Messenger^{6,7}, M. S. Meyer⁵, H. Miao¹⁹, C. Michel³¹, L. Milano^{4ab}, J. Miller²,
Y. Minenkov^{51a}, Y. Mino³⁴, V. P. Mitrofanov²⁷, G. Mitselmakher¹⁰, R. Mittleman²⁰,
O. Miyakawa⁶³, B. Moe⁸, P. Moesta¹⁵, M. Mohan¹⁷, S. D. Mohanty²⁵, S. R. P. Mohapatra⁴⁰,
D. Moraru¹⁴, G. Moreno¹⁴, N. Morgado³¹, A. Morgia^{51ab}, S. Mosca^{4ab}, V. Moscatelli^{12a},
K. Mossavi^{6,7}, B. Mours³, C. M. Mow–Lowry⁴⁸, G. Mueller¹⁰, S. Mukherjee²⁵,
A. Mullavey⁴⁸, H. Müller-Ebhardt^{6,7}, J. Munch⁶⁴, P. G. Murray², T. Nash¹, R. Nawrodt²,
J. Nelson², I. Neri^{33ab}, G. Newton², E. Nishida⁶³, A. Nishizawa⁶³, F. Nocera¹⁷, D. Nolting⁵,
E. Ochsner³⁹, J. O’Dell³⁷, G. H. Ogin¹, R. G. Oldenburg⁸, B. O’Reilly⁵,
R. O’Shaughnessy³⁰, C. Osthelder¹, C. D. Ott³⁴, D. J. Ottaway⁶⁴, R. S. Ottens¹⁰,
H. Overmier⁵, B. J. Owen³⁰, A. Page¹³, G. Pagliaroli^{51ac}, L. Palladino^{51ac}, C. Palomba^{12a},
Y. Pan³⁹, C. Pankow¹⁰, F. Paoletti^{23a,17}, M. A. Papa^{15,8}, A. Parameswaran¹, S. Pardi^{4ab},
M. Parisi^{4ab}, A. Pasqualetti¹⁷, R. Passaquieti^{23ab}, D. Passuello^{23a}, P. Patel¹, D. Pathak⁵⁰,
M. Pedraza¹, L. Pekowsky³⁶, S. Penn⁷¹, C. Peralta¹⁵, A. Perreca¹³, G. Persichetti^{4ab},
M. Phelps¹, M. Pichot^{28a}, M. Pickenpack^{6,7}, F. Piergiovanni^{41ab}, M. Pietka^{38d}, L. Pinard³¹,
I. M. Pinto⁷², M. Pitkin², H. J. Pletsch^{6,7}, M. V. Plissi², J. Podkaminer⁷¹, R. Poggiani^{23ab},
J. Pödl^{6,7}, F. Postiglione⁵², M. Prato⁴⁷, V. Predoi⁵⁰, L. R. Price⁸, M. Prijatelj^{6,7},
M. Principe⁷², S. Privitera¹, R. Prix^{6,7}, G. A. Prodi^{57ab}, L. Prokhorov²⁷, O. Puncken^{6,7},
M. Punturo^{33a}, P. Puppo^{12a}, V. Quetschke²⁵, F. J. Raab¹⁴, D. S. Rabeling^{24ab}, I. Rácz⁵⁴,
H. Radkins¹⁴, P. Raffai⁶¹, M. Rakhmanov²⁵, C. R. Ramet⁵, B. Rankins⁴², P. Rapagnani^{12ab},
V. Raymond⁵⁹, V. Re^{51ab}, K. Redwine²², C. M. Reed¹⁴, T. Reed⁷³, T. Regimbau^{28a},
S. Reid², D. H. Reitze¹⁰, F. Ricci^{12ab}, R. Riesen⁵, K. Riles⁴⁵, P. Roberts⁷⁴,
N. A. Robertson^{1,2}, F. Robinet^{29a}, C. Robinson⁵⁰, E. L. Robinson¹⁵, A. Rocchi^{51a},
S. Roddy⁵, L. Rolland³, J. Rollins²², J. D. Romano²⁵, R. Romano^{4ac}, J. H. Romie⁵,
D. Rosińska^{38cf}, C. Röver^{6,7}, S. Rowan², A. Rüdiger^{6,7}, P. Ruggi¹⁷, K. Ryan¹⁴, S. Sakata⁶³,
M. Sakosky¹⁴, F. Salemi^{6,7}, M. Salit⁵⁹, L. Sammut⁴⁹, L. Sancho de la Jordana⁶⁵,
V. Sandberg¹⁴, V. Sannibale¹, L. Santamaría¹⁵, I. Santiago-Prieto², G. Santostasi⁷⁵,
S. Saraf⁷⁶, B. Sassolas³¹, B. S. Sathyaprakash⁵⁰, S. Sato⁶³, M. Satterthwaite⁴⁸,
P. R. Saulson³⁶, R. Savage¹⁴, R. Schilling^{6,7}, S. Schlamminger⁸, R. Schnabel^{6,7},
R. M. S. Schofield³⁵, B. Schulz^{6,7}, B. F. Schutz^{15,50}, P. Schwinberg¹⁴, J. Scott²,
S. M. Scott⁴⁸, A. C. Searle¹, F. Seifert¹, D. Sellers⁵, A. S. Sengupta¹, D. Sentenac¹⁷,
A. Sergeev⁶⁷, D. A. Shaddock⁴⁸, M. Shaltev^{6,7}, B. Shapiro²⁰, P. Shawhan³⁹,
T. Shihan Weerathunga²⁵, D. H. Shoemaker²⁰, A. Sibley⁵, X. Siemens⁸, D. Sigg¹⁴,
A. Singer¹, L. Singer¹, A. M. Sintes⁶⁵, G. Skelton⁸, B. J. J. Slagmolen⁴⁸, J. Slutsky¹¹,
J. R. Smith⁷⁷, M. R. Smith¹, N. D. Smith²⁰, R. Smith¹³, K. Somiya³⁴, B. Sorazu²,
J. Soto²⁰, F. C. Speirits², L. Sperandio^{51ab}, M. Stefszky⁴⁸, A. J. Stein²⁰, J. Steinlechner^{6,7},
S. Steinlechner^{6,7}, S. Steplewski³², A. Stochino¹, R. Stone²⁵, K. A. Strain², S. Strigin²⁷,
A. S. Stroeer⁴³, R. Sturani^{41ab}, A. L. Stuver⁵, T. Z. Summerscales⁷⁴, M. Sung¹¹,
S. Susmithan¹⁹, P. J. Sutton⁵⁰, B. Swinkels¹⁷, G. P. Szokoly⁶¹, M. Tacca¹⁷, D. Talukder³²,

D. B. Tanner¹⁰, S. P. Tarabrin^{6,7}, J. R. Taylor^{6,7}, R. Taylor¹, P. Thomas¹⁴, K. A. Thorne⁵,
K. S. Thorne³⁴, E. Thrane⁵⁶, A. Thüring^{7,6}, C. Titsler³⁰, K. V. Tokmakov⁶⁸, A. Toncelli^{23ab},
M. Tonelli^{23ab}, O. Torre^{23ac}, C. Torres⁵, C. I. Torrie^{1,2}, E. Tournefier³, F. Travasso^{33ab},
G. Traylor⁵, M. Trias⁶⁵, K. Tseng⁹, L. Turner¹, D. Ugolini⁷⁸, K. Urbanek⁹, H. Vahlbruch^{7,6},
B. Vaishnav²⁵, G. Vajente^{23ab}, M. Vallisneri³⁴, J. F. J. van den Brand^{24ab},
C. Van Den Broeck⁵⁰, S. van der Putten^{24a}, M. V. van der Sluys⁵⁹, A. A. van Veggel²,
S. Vass¹, M. Vasuth⁵⁴, R. Vaulin⁸, M. Vavoulidis^{29a}, A. Vecchio¹³, G. Vedovato^{57c},
J. Veitch⁵⁰, P. J. Veitch⁶⁴, C. Veltkamp^{6,7}, D. Verkindt³, F. Vetrano^{41ab}, A. Viceré^{41ab},
A. E. Villar¹, J.-Y. Vinet^{28a}, H. Vocca^{33a}, C. Vorvick¹⁴, S. P. Vyachanin²⁷,
S. J. Waldman²⁰, L. Wallace¹, A. Wanner^{6,7}, R. L. Ward²¹, M. Was^{29a}, P. Wei³⁶,
M. Weinert^{6,7}, A. J. Weinstein¹, R. Weiss²⁰, L. Wen^{34,19}, S. Wen⁵, P. Wessels^{6,7}, M. West³⁶,
T. Westphal^{6,7}, K. Wette^{6,7}, J. T. Whelan⁷⁹, S. E. Whitcomb¹, D. White⁵³,
B. F. Whiting¹⁰, C. Wilkinson¹⁴, P. A. Willems¹, H. R. Williams³⁰, L. Williams¹⁰,
B. Willke^{6,7}, L. Winkelmann^{6,7}, W. Winkler^{6,7}, C. C. Wipf²⁰, A. G. Wiseman⁸, G. Woan²,
R. Wooley⁵, J. Worden¹⁴, J. Yablon⁵⁹, I. Yakushin⁵, H. Yamamoto¹, K. Yamamoto^{6,7},
H. Yang³⁴, D. Yeaton-Massey¹, S. Yoshida⁸⁰, P. Yu⁸, M. Yvert³, M. Zanolin⁶², L. Zhang¹,
Z. Zhang¹⁹, C. Zhao¹⁹, N. Zotov⁷³, M. E. Zucker²⁰, J. Zweizig¹

(The LIGO Scientific Collaboration & The Virgo Collaboration)

S. Buchner^{81,82}, A. Hotan⁸³, J. Palfreyman⁸⁴

-
- ¹LIGO - California Institute of Technology, Pasadena, CA 91125, USA
- ²University of Glasgow, Glasgow, G12 8QQ, United Kingdom
- ³Laboratoire d'Annecy-le-Vieux de Physique des Particules (LAPP), Université de Savoie, CNRS/IN2P3, F-74941 Annecy-Le-Vieux, France
- ⁴INFN, Sezione di Napoli ^a; Università di Napoli 'Federico II' ^b Complesso Universitario di Monte S. Angelo, I-80126 Napoli; Università di Salerno, Fisciano, I-84084 Salerno ^c, Italy
- ⁵LIGO - Livingston Observatory, Livingston, LA 70754, USA
- ⁶Albert-Einstein-Institut, Max-Planck-Institut für Gravitationsphysik, D-30167 Hannover, Germany
- ⁷Leibniz Universität Hannover, D-30167 Hannover, Germany
- ⁸University of Wisconsin–Milwaukee, Milwaukee, WI 53201, USA
- ⁹Stanford University, Stanford, CA 94305, USA
- ¹⁰University of Florida, Gainesville, FL 32611, USA
- ¹¹Louisiana State University, Baton Rouge, LA 70803, USA
- ¹²INFN, Sezione di Roma ^a; Università 'La Sapienza' ^b, I-00185 Roma, Italy
- ¹³University of Birmingham, Birmingham, B15 2TT, United Kingdom
- ¹⁴LIGO - Hanford Observatory, Richland, WA 99352, USA
- ¹⁵Albert-Einstein-Institut, Max-Planck-Institut für Gravitationsphysik, D-14476 Golm, Germany
- ¹⁶Montana State University, Bozeman, MT 59717, USA
- ¹⁷European Gravitational Observatory (EGO), I-56021 Cascina (PI), Italy
- ¹⁸Carleton College, Northfield, MN 55057, USA
- ¹⁹University of Western Australia, Crawley, WA 6009, Australia
- ²⁰LIGO - Massachusetts Institute of Technology, Cambridge, MA 02139, USA
- ²¹Laboratoire AstroParticule et Cosmologie (APC) Université Paris Diderot, CNRS: IN2P3, CEA: DSM/IRFU, Observatoire de Paris, 10 rue A.Domon et L.Duquet, 75013 Paris - France
- ²²Columbia University, New York, NY 10027, USA
- ²³INFN, Sezione di Pisa ^a; Università di Pisa ^b; I-56127 Pisa; Università di Siena, I-53100 Siena ^c, Italy
- ²⁴Nikhef, Science Park, Amsterdam, the Netherlands ^a; VU University Amsterdam, De Boelelaan 1081, 1081 HV Amsterdam, the Netherlands ^b
- ²⁵The University of Texas at Brownsville and Texas Southmost College, Brownsville, TX 78520, USA
- ²⁶San Jose State University, San Jose, CA 95192, USA
- ²⁷Moscow State University, Moscow, 119992, Russia

²⁸Université Nice-Sophia-Antipolis, CNRS, Observatoire de la Côte d’Azur, F-06304 Nice^a; Institut de Physique de Rennes, CNRS, Université de Rennes 1, 35042 Rennes^b, France

²⁹LAL, Université Paris-Sud, IN2P3/CNRS, F-91898 Orsay^a; ESPCI, CNRS, F-75005 Paris^b, France

³⁰The Pennsylvania State University, University Park, PA 16802, USA

³¹Laboratoire des Matériaux Avancés (LMA), IN2P3/CNRS, F-69622 Villeurbanne, Lyon, France

³²Washington State University, Pullman, WA 99164, USA

³³INFN, Sezione di Perugia^a; Università di Perugia^b, I-06123 Perugia, Italy

³⁴Caltech-CaRT, Pasadena, CA 91125, USA

³⁵University of Oregon, Eugene, OR 97403, USA

³⁶Syracuse University, Syracuse, NY 13244, USA

³⁷Rutherford Appleton Laboratory, HSIC, Chilton, Didcot, Oxon OX11 0QX United Kingdom

³⁸IM-PAN 00-956 Warsaw^a; Astronomical Observatory Warsaw University 00-478 Warsaw^b; CAMK-PAN 00-716 Warsaw^c; Białystok University 15-424 Białystok^d; IPJ 05-400 Świerk-Otwock^e; Institute of Astronomy 65-265 Zielona Góra^f, Poland

³⁹University of Maryland, College Park, MD 20742 USA

⁴⁰University of Massachusetts - Amherst, Amherst, MA 01003, USA

⁴¹INFN, Sezione di Firenze, I-50019 Sesto Fiorentino^a; Università degli Studi di Urbino ‘Carlo Bo’, I-61029 Urbino^b, Italy

⁴²The University of Mississippi, University, MS 38677, USA

⁴³NASA/Goddard Space Flight Center, Greenbelt, MD 20771, USA

⁴⁴Tsinghua University, Beijing 100084 China

⁴⁵University of Michigan, Ann Arbor, MI 48109, USA

⁴⁶Charles Sturt University, Wagga Wagga, NSW 2678, Australia

⁴⁷INFN, Sezione di Genova; I-16146 Genova, Italy

⁴⁸Australian National University, Canberra, 0200, Australia

⁴⁹The University of Melbourne, Parkville VIC 3010, Australia

⁵⁰Cardiff University, Cardiff, CF24 3AA, United Kingdom

⁵¹INFN, Sezione di Roma Tor Vergata^a; Università di Roma Tor Vergata, I-00133 Roma^b; Università dell’Aquila, I-67100 L’Aquila^c, Italy

⁵²University of Salerno, I-84084 Fisciano (Salerno), Italy and INFN (Sezione di Napoli), Italy

⁵³The University of Sheffield, Sheffield S10 2TN, United Kingdom

⁵⁴RMKI, H-1121 Budapest, Konkoly Thege Miklós út 29-33, Hungary

-
- ⁵⁵Inter-University Centre for Astronomy and Astrophysics, Pune - 411007, India
- ⁵⁶University of Minnesota, Minneapolis, MN 55455, USA
- ⁵⁷INFN, Gruppo Collegato di Trento^a and Università di Trento^b, I-38050 Povo, Trento, Italy; INFN, Sezione di Padova^c and Università di Padova^d, I-35131 Padova, Italy
- ⁵⁸California Institute of Technology, Pasadena, CA 91125, USA
- ⁵⁹Northwestern University, Evanston, IL 60208, USA
- ⁶⁰The University of Texas at Austin, Austin, TX 78712, USA
- ⁶¹Eötvös Loránd University, Budapest, 1117 Hungary
- ⁶²Embry-Riddle Aeronautical University, Prescott, AZ 86301 USA
- ⁶³National Astronomical Observatory of Japan, Tokyo 181-8588, Japan
- ⁶⁴University of Adelaide, Adelaide, SA 5005, Australia
- ⁶⁵Universitat de les Illes Balears, E-07122 Palma de Mallorca, Spain
- ⁶⁶University of Southampton, Southampton, SO17 1BJ, United Kingdom
- ⁶⁷Institute of Applied Physics, Nizhny Novgorod, 603950, Russia
- ⁶⁸University of Strathclyde, Glasgow, G1 1XQ, United Kingdom
- ⁶⁹Southern University and A&M College, Baton Rouge, LA 70813, USA
- ⁷⁰University of Rochester, Rochester, NY 14627, USA
- ⁷¹Hobart and William Smith Colleges, Geneva, NY 14456, USA
- ⁷²University of Sannio at Benevento, I-82100 Benevento, Italy and INFN (Sezione di Napoli), Italy
- ⁷³Louisiana Tech University, Ruston, LA 71272, USA
- ⁷⁴Andrews University, Berrien Springs, MI 49104 USA
- ⁷⁵McNeese State University, Lake Charles, LA 70609 USA
- ⁷⁶Sonoma State University, Rohnert Park, CA 94928, USA
- ⁷⁷California State University Fullerton, Fullerton CA 92831 USA
- ⁷⁸Trinity University, San Antonio, TX 78212, USA
- ⁷⁹Rochester Institute of Technology, Rochester, NY 14623, USA
- ⁸⁰Southeastern Louisiana University, Hammond, LA 70402, USA
- ⁸¹Hartebeesthoek Radio Astronomy Observatory, PO Box 443, Krugersdorp, 1740, South Africa
- ⁸²School of Physics, University of the Witwatersrand, Private Bag 3, WITS 2050, South Africa
- ⁸³CSIRO Astronomy and Space Science, PO Box 76, Epping NSW 1710, Australia
- ⁸⁴School of Maths and Physics University of Tasmania, GPO Box 1653 Hobart, Tasmania 7001 Australia

ABSTRACT

We present direct upper limits on continuous gravitational wave emission from the Vela pulsar using data from the Virgo detector’s second science run. These upper limits have been obtained using three independent methods that assume the gravitational wave emission follows the radio timing. Two of the methods produce frequentist upper limits for an assumed known orientation of the star’s spin axis and value of the wave polarization angle of, respectively, 1.9×10^{-24} and 2.2×10^{-24} , with 95% confidence. The third method, under the same hypothesis, produces a Bayesian upper limit of 2.1×10^{-24} , with 95% degree of belief. These limits are below the indirect *spin-down limit* of 3.3×10^{-24} for the Vela pulsar, defined by the energy loss rate inferred from observed decrease in Vela’s spin frequency, and correspond to a limit on the star ellipticity of $\sim 10^{-3}$. Slightly less stringent results, but still well below the spin-down limit, are obtained assuming the star’s spin axis inclination and the wave polarization angles are unknown.

Subject headings: gravitational waves - pulsars: general

1. Introduction

We describe here a search for continuous gravitational radiation from the Vela pulsar (PSR B0833–45, PSR J0835–4510) in data from the Virgo detector VSR2 run, which began on 2009 July 7 and ended on 2010 January 8. Continuous gravitational waves (CW) can be emitted by a rotating neutron star through a variety of possible mechanisms, including non-axisymmetry of its mass distribution, giving rise to a time-varying quadrupole moment. Such emission would imply loss of rotational energy and decrease in spin frequency. Hence a pulsar’s observed frequency spin-down can be used to place an indirect upper limit on its gravitational wave emission, named *spin-down limit*. While a recent search for CW radiation using LIGO data has been carried out for more than 100 known pulsars (Abbott et al. 2010), the resulting upper limits have beaten the spin-down limit for only the Crab pulsar (Abbott et al. 2008, 2010). A search over LIGO data for CW signals from the non-pulsing neutron star in the supernova remnant Cassiopeia A has established an upper limit on the signal amplitude over a wide range of frequencies which is below the *indirect* limit derived from energy conservation (Abadie et al. 2010). In this article we present upper limits on CW emission from the Vela pulsar that lie below its spin-down limit, making Vela only the second pulsar for which this experimental milestone has been achieved. The only previous targeted search for CW emission from the Vela pulsar was in CLIO data over the period 2007

February 12–28, which produced an upper limit of $\sim 5.3 \times 10^{-20}$, several orders of magnitude above the spin-down limit (Akutsu et al. 2008).

Vela is observed to pulsate ($f_{rot} \simeq 11.19$ Hz) in radio, optical, X-ray and γ -ray radiation and is associated with the Vela supernova remnant. The association of the pulsar to the supernova remnant was made in 1968 (Large et al. 1968) and was the first direct observational proof that supernovae can produce neutron stars. The Vela spin-down rate is $\dot{f}_{rot} \simeq -1.56 \times 10^{-11}$ Hz s $^{-1}$, corresponding to a kinetic energy loss of $\dot{E}_{sd} \simeq 6.9 \times 10^{29}$ W, where the canonical value for a neutron star’s moment of inertia, $I = 10^{38}$ kg m 2 , has been assumed. This loss of energy is due to various mechanisms, including magnetic dipole radiation, acceleration of charged particles in the pulsar magnetosphere and possibly the emission of gravitational waves. In this analysis we assume a tri-axial neutron star rotating around a principal axis of inertia, so that the gravitational wave (GW) signal frequency is $f = 2f_{rot}$ (see Section 2). With an estimated distance from the Earth of ~ 290 pc (Dodson et al. 2003), Vela is one of the nearest known pulsars. Assuming that all the observed spin-down is due to the emission of gravitational waves, we obtain the spin-down limit $h_0^{sd} = 3.29 \times 10^{-24}$ for GW tensor amplitude at the Earth. With an estimated age of $\sim 11\,000$ yr (Caraveo & Bignami 1989), Vela is relatively young and could, in principle, have a significant residual non-axisymmetry from its formation. The spin-down limit on the signal amplitude can be converted into an upper limit on the star’s equatorial ellipticity ϵ (see Eq. 15). For Vela we have $\epsilon^{sd} = 1.8 \times 10^{-3}$. This value is far larger than the maximum allowed by standard equations of state for neutron star matter (Horowitz & Kadau 2009), but is comparable to the maximum value foreseen by some exotic equations of state (Owen 2005; Lin 2007; Haskell et al. 2007). Because of very effective seismic isolation (Acernese et al. 2010), Vela’s GW emission frequency ($f \simeq 22.38$ Hz) is within the sensitive band of the Virgo detector; this frequency range is inaccessible to all other gravitational wave detectors to date.

Vela is a particularly glitchy pulsar, with an average glitch rate of $\sim 1/3$ yr $^{-1}$, making it important to know whether or not a glitch occurred during the VSR2 run. Vela is regularly

Table 1. Position and estimated distance of Vela pulsar. For the position, parentheses give the 1σ error on the final digit as produced by the *TEMPO2* fit; for the distance, the uncertainty estimated in (Dodson et al. 2003) is quoted. Positional parameters refer to epoch (MJD) 54620.

α	δ	d [pc]
$08^h 35^m 20.75438(3)^s$	$-45^\circ 10' 32''.9507(7)$	$287 (-17, +19)$

monitored by both the Hobart radio telescope in Tasmania and the Hartebeesthoek radio telescope in South Africa. According to their observations, no glitch occurred during the time span of VSR2. Prior to VSR2 it last glitched on 2007 August 1, and it has since glitched on 2010 July 31 (Buchner 2010). Observations from the Hobart and Hartebeesthoek telescopes have also been used to produce updated ephemerides for Vela, which are important given Vela’s relatively large timing noise. If timing noise is a consequence of fluctuations in the star’s rotation frequency, not taking it into account would result in an increasing mismatch over time between the signal and template phases, thus producing a sensitivity loss in a coherent search. In this search updated ephemerides have been computed using the pulsar software *TEMPO2* starting from the set of times of arrival (TOAs) of the electromagnetic pulses observed by the Hobart and Hartebeesthoek telescopes covering the whole duration of the VSR2 run. Including in the fitting process up to the second derivative of frequency is enough in order to have flat post-fit residuals. The post-fit position and frequency parameters are shown in Table 1 and Table 2 respectively. The corresponding post-fit residuals rms amounts to a negligible $100 \mu\text{s}$.

Recent Chandra X-ray observations provide accurate determination of the orientation of the Vela spin axis. In (Ng & Romani 2008) estimates of the pulsar wind nebula’s “position angle”, ψ_P , and inclination ι_P are given:

$$\begin{aligned}\psi_P &= 130.63^\circ \pm 0.05^\circ, \\ \iota_P &= 63.6^\circ \pm 0.6^\circ.\end{aligned}\tag{1}$$

The “position angle” is related to the gravitational wave polarization angle ψ (see Section 2) by either $\psi = 180^\circ + \psi_P$ or $\psi = \psi_P$ depending on the unknown spin direction. Our analyses are insensitive to rotations of ψ by integer multiples of 90° , so the spin direction is not needed. The inclination angle calculated from the pulsar wind nebula ι_P is taken to be the same as that of the pulsar ι . The physics of pulsar wind nebulae is complex, and a model leading to the above fits has several uncertainties. Thus we perform separate searches

Table 2. Spin frequency, spin-down rate and estimated age of Vela pulsar. Parentheses give the 1σ error on the final digit of spin frequency and spin-down rate estimations as produced by the *TEMPO2* fit. Rotational parameters refer to epoch (MJD) 54620. The quoted precision is enough to determine the rotational phase to within about 0.012 cycles.

f_{rot} [Hz]	\dot{f}_{rot} [Hz s ⁻¹]	\ddot{f}_{rot} [Hz s ⁻²]	Age [yr]
11.19057302331(9)	$-1.5583876(4) \times 10^{-11}$	$4.9069(9) \times 10^{-22}$	11 000

for the GW signal from Vela, both assuming that the angles ψ and ι are known within the above uncertainties, and assuming that they are unknown.

The remainder of this paper is organized as follows. In Section 2 we summarize the characteristics of the GW signals for which we search. In Section 3 we describe the data set used for the analysis. In Section 4 we briefly describe the three analysis methods used. In Section 5 we present the results of the analysis. In Section 6 we provide conclusions. Some more details on the analysis methods are given in the Appendices.

2. The GW signal

The continuous GW signal emitted by a triaxial neutron star rotating around a principal axis of inertia as seen from Earth is described by the following tensor metric perturbation:

$$\mathbf{h}(t) = h_+(t) \mathbf{e}_+ + h_\times(t) \mathbf{e}_\times, \quad (2)$$

where

$$h_+(t) = h_0 \left(\frac{1 + \cos^2 \iota}{2} \right) \cos \Phi(t) \quad (3)$$

$$h_\times(t) = h_0 \cos \iota \sin \Phi(t), \quad (4)$$

and \mathbf{e}_+ and \mathbf{e}_\times are the two basis polarization tensors. They are defined, see *e.g.* (Misner et al. 1973), in terms of unit orthogonal vectors \mathbf{e}_x and \mathbf{e}_y where \mathbf{e}_x is along the x-axis of the wave frame, defined as the cross product $\hat{s} \times \hat{n}$ between the source spin direction \hat{s} and the source direction \hat{n} in the solar system barycenter (SSB).

The angle ι is the inclination of the star’s rotation axis with respect to the line of sight and $\Phi(t)$ is the signal phase function, where t is the detector time, while the amplitude h_0 is given by

$$h_0 = \frac{4\pi^2 G}{c^4} \frac{I_{zz} \epsilon f^2}{d}, \quad (5)$$

where I_{zz} is the star moment of inertia with respect to the rotation axis, the equatorial ellipticity ϵ is defined, in terms of principal moments of inertia, as $\epsilon = \frac{I_{xx} - I_{yy}}{I_{zz}}$, d is the star distance and f is the signal frequency. As the time-varying components of the mass quadrupole moment tensor are periodic with period half the star rotation period, it follows that $f = 2f_{rot}$.

The GW strain at the detector can be described as

$$h(t) = h_+(t) F_+(t; \psi) + h_\times(t) F_\times(t; \psi), \quad (6)$$

where the two beam-pattern functions, which are periodic functions of time with period of one sidereal day, are given by

$$F_+(t; \psi) = a(t) \cos 2\psi + b(t) \sin 2\psi \quad (7)$$

$$F_\times(t; \psi) = b(t) \cos 2\psi - a(t) \sin 2\psi. \quad (8)$$

The two functions $a(t), b(t)$ depend on the source position in the sky and on the detector position and orientation on the Earth. Their time dependency is sinusoidal and cosinusoidal with arguments $\Omega_\oplus t$ and $2\Omega_\oplus t$, where Ω_\oplus is the Earth angular rotation frequency; ψ is the wave polarization angle defined as the angle from $\hat{z} \times \hat{n}$ to the x-axis of the wave frame, measured counterclockwise respect to \hat{n} , where \hat{z} is the direction of the North celestial pole (see, *e.g.*, the plot in (Prix & Krishnan 2009)). The effect of detector response on a monochromatic signal with angular frequency ω_0 is to introduce an amplitude and phase modulation which determine a split of the signal power into five frequencies, $\omega_0, \omega_0 \pm \Omega_\oplus, \omega_0 \pm 2\Omega_\oplus$. The distribution of power among the five bands depends on the source and detector angular parameters. In Fig. 1 the power spectrum at the Virgo detector of an hypothetical monochromatic signal coming from the location of the Vela pulsar is shown for two assumed polarizations (pure “+” linear polarization and circular left handed polarization).

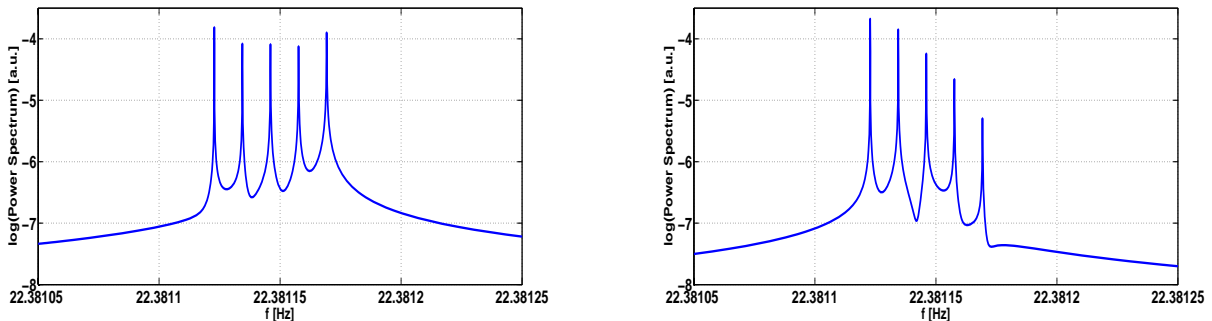


Fig. 1.— Power spectrum of an hypothetical monochromatic signal coming from the location of the Vela pulsar as seen from the Virgo detector. Left plot refers to a purely + signal; right plot to a circularly (left handed) polarized signal.

To a very good approximation the SSB can be used as an inertial reference frame in which to define the signal phase. In this frame, with barycentric time T , the signal phase is

$$\Phi(T) = \Phi_0 + 2\pi f_0 (T - T_0), \quad (9)$$

where the signal intrinsic frequency f_0 is a function of time due to the spin-down:

$$f_0(T) = f^{(0)} + \sum_{n=1}^2 \frac{f^{(n)}}{n!} (T - T_0)^n, \quad (10)$$

where $f^{(n)} = \frac{d^n f_0}{dT^n}|_{T=T_0}$. The time at the detector, t , differs from T due to the relative motion between the source and the detector and to some relativistic effects. Considering only isolated neutron stars we have the well-known relation (Lyne & Graham-Smith 1998; Hobbs et al. 2006; Edwards et al. 2006)

$$T = t + \Delta_R + \Delta_E + \Delta_S, \quad (11)$$

where

$$\Delta_R = \frac{\vec{r} \cdot \hat{n}}{c} \quad (12)$$

is the classical Roemer delay, which gives the main contribution (\vec{r} is the vector identifying the detector position in the SSB, while \hat{n} is the unit vector toward the source). The term Δ_E is the Einstein delay which is the sum of two contributions, one due to the gravitational redshift produced by the Sun and the other due to the time dilation produced by the Earth's motion. Δ_S is the Shapiro delay due to the curvature of space-time near the Sun. Expressing the signal phase in the detector frame, by using Eq. 11, we can write the signal frequency at the detector as

$$f(t) = \frac{1}{2\pi} \frac{d\Phi(t)}{dt} \simeq f_0(t) \left(1 + \frac{\vec{v} \cdot \hat{n}}{c} \right) + \text{rel. corr.}, \quad (13)$$

where \vec{v} is the detector velocity vector and terms of order $|f^{(1)} \frac{\vec{r} \cdot \hat{n}}{c}|$ or smaller have been omitted from the equation (though they are included in the analyses).

A useful quantity to which to compare the upper limit on signal strength set in a given analysis is the so-called spin-down limit. It is computed (Abbott et al. 2007) assuming that all the observed spin-down is due to the emission of GW:

$$h_0^{sd} = 8.06 \times 10^{-19} I_{38} d_{\text{kpc}}^{-1} \sqrt{\frac{|(\dot{f}_{rot}/\text{Hz s}^{-1})|}{(f_{rot}/\text{Hz})}}, \quad (14)$$

where I_{38} is the star's moment of inertia in units of 10^{38} kg m^2 and d_{kpc} is the star's distance from the Sun in kiloparsecs. It is an absolute upper limit to the amplitude of the GW signal that could be emitted by the star, where electromagnetic radiation is neglected. The spin-down limit on the signal amplitude corresponds to an upper limit on the star's ellipticity given by

$$\epsilon^{sd} = 0.237 \left(\frac{h_0^{sd}}{10^{-24}} \right) I_{38}^{-1} (f_{rot}/\text{Hz})^{-2} d_{\text{kpc}}. \quad (15)$$

The Vela pulsar has a measured braking index $n \simeq 1.4$ (Lyne et al 1996) and this, together with the estimation of its age, can be used to compute a stricter indirect limit on the signal amplitude (Palomba 2000), which only holds under the assumption that the spin-down is due to the combination of emission of GW and magnetic dipole radiation, about 4 times lower than the spin-down limit.

Achieving sensitivity better than the spin-down limit is an important milestone toward probing neutron star structure via gravitational waves.

3. Instrumental performance in the VSR2 run

We have analyzed calibrated strain data from the Virgo VSR2 run. This run (started in coincidence with the start of the LIGO S6 data run) began on 2009 July 7 21:00:00 UTC (GPS 931035615) and ended on 2010 January 8 22:00:01 UTC (GPS 947023216). The duty cycle was 80.4%, resulting in a total of ~ 149 days of *science mode* data, divided among 379 segments. Science mode is a flag used to indicate when the interferometer is locked and freely running at its working point, with all the controls active and no human intervention. In Fig. 2 the fraction of total time covered by science data segments with duration longer than a given value is plotted. The longest segment lasts ~ 88 hours.

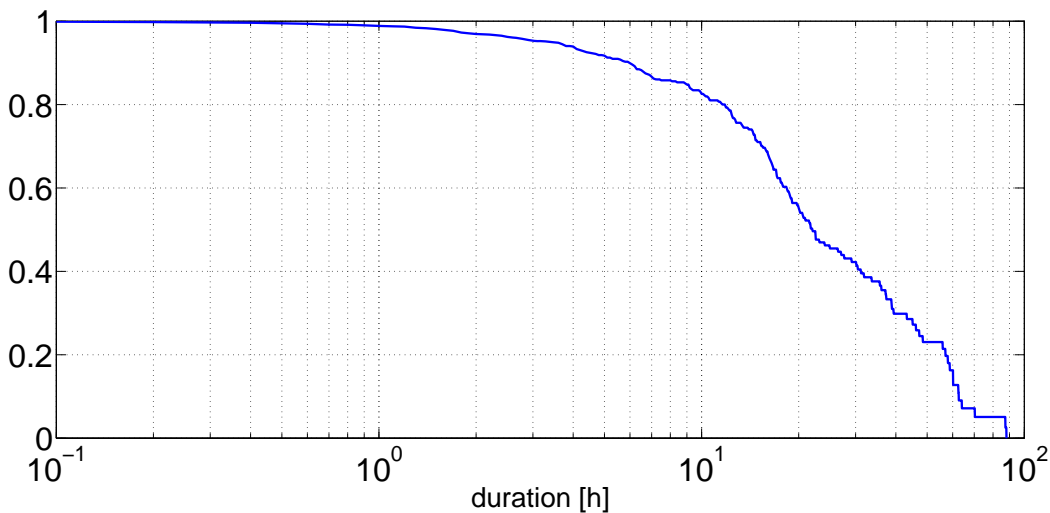


Fig. 2.— Fraction of the total time covered by science data segments with duration larger than a given time.

The detector showed a good sensitivity around the expected Vela signal frequency during the entire run. The sensitivity was typically within a factor of two of the target Virgo design sensitivity (Accadia *et al.* 2010). Figure 3 shows the estimation of the power spectrum of the data, computed through an average of $\sim 1,000$ s periodograms after removal of some large outliers (see Section 4.3.1), on a 0.8 Hz frequency band around the expected frequency of the GW signal from the Vela pulsar for the entire VSR2 run. An instrumental disturbance right at the Vela signal frequency degraded the sensitivity by $\sim 20\%$ with respect to the

background. The source of this disturbance was seismic noise produced by the engine of the chiller pumps that circulate coolant fluid for the laser of the mirror thermal compensation system and it has been removed during the next Virgo VSR3 run.

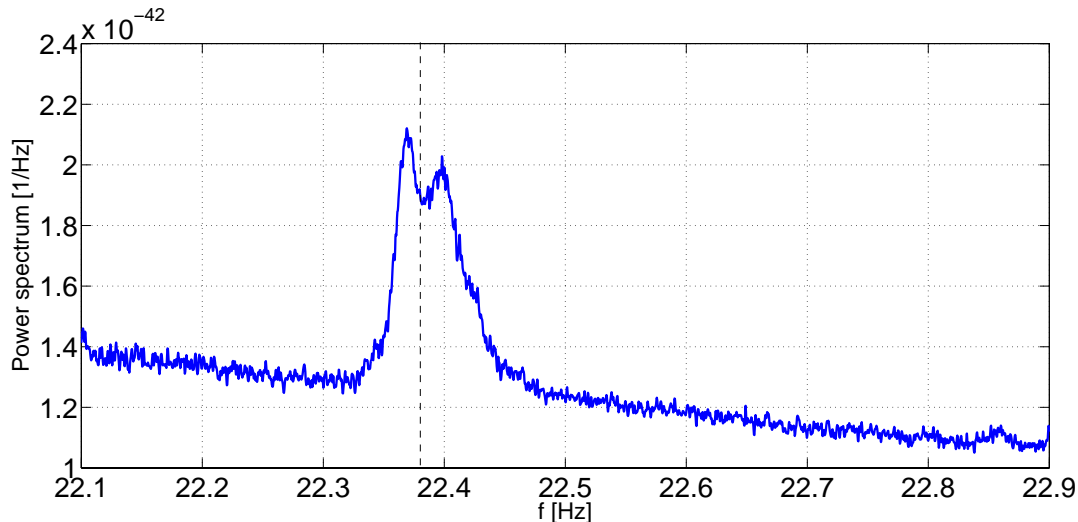


Fig. 3.— Estimation of the power spectrum of VSR2 data in a 0.8Hz band around the expected Vela signal frequency. The expected signal frequency (vertical dashed line) is right in the middle of the frequency band affected by an instrumental disturbance, see text for more details.

The data used in the analysis have been produced using the most up-to-date calibration parameters and reconstruction procedure. The associated systematic error amounts to 5.5% in amplitude and ~ 50 mrad in phase (Accadia *et al.* 2010) over the frequency range between ~ 10 Hz and ~ 1 kHz, with lower uncertainties at the Vela frequency. The reconstructed data have a sampling rate of 20 000 Hz. However two more reconstructed data streams, sampled respectively at 16 384 Hz and 4 096 Hz, were also produced to be consistent with LIGO/GEO sampling rates.

4. The search methods

Three different and largely independent analysis methods have been applied to this search: 1) a complex heterodyne method using Bayesian formalism and a Markov chain Monte Carlo (Abbott *et al.* 2010); 2) a time-domain matched filter method using the \mathcal{F} -statistic (Jaranowski *et al.* 1998) and a new extension known as the \mathcal{G} -statistic (Jaranowski & Królak 2010); and 3) a matched filter method applied to the signal’s Fourier components

at the five frequencies to which the signal is spread by the sidereal modulation (Astone et al. 2010).

There are several reasons to use different methods in the search for CW signals, provided they have comparable performance. First, it makes it easier to cross-check each method by comparing the analysis outputs, even at intermediate steps. Second, different methods can be more suitable, or efficient, for given characteristics of the data to be analyzed, or for given characteristics of the signal emitted by a source; *e.g.* a method can be more robust against noise non-stationarity with respect to another. Third, in case of detection with a given analysis it will be of paramount importance to confirm the detection with one or more independent analyses.

In the analyses described in this paper we observe consistent results from the three methods, which provide valuable cross-checks.

All the analyses clean the data in some way to remove large transient outliers. This is necessary, as large short-duration transients will skew noise estimates and adversely affect results. The amount of data removed during cleaning is negligible compared to the total data span and would produce a decrease of the signal-to-noise ratio of a signal present in the data of less than 1%.

Among the three methods two different approaches have been used towards setting upper limits. In the heterodyne method the posterior probability for the signal parameters is calculated, from which degree of belief (or credibility) regions can be set to give limits on particular parameters (*e.g.*, an upper limit on h_0 can be set by finding the value that bounds a given percentage of the probability). In the two other analyses a frequentist approach is used and upper limits are set through Monte Carlo methods where many simulated signals with different amplitude and randomly varying parameters and frequency near the expected one from the Vela are added to the data. These two approaches should produce quantitatively similar results, see for example (Abbott et al. 2004), but they are answering different questions and therefore cannot be meaningfully combined.

The three analysis methods are described in the following sections of this paper.

4.1. Complex heterodyne

This method, developed in (Dupuis & Woan 2005), provides a way to reduce the search dataset to a manageable size, and use it to perform Bayesian parameter estimation of the unknown signal parameters.

4.1.1. Data reduction

The known signal phase evolution (Eq. 9) is used to heterodyne the data, changing the time series detector data $x(t) = h(t) + n(t)$, where $h(t)$ is the signal given by Eq. 6 and $n(t)$ is the noise, to

$$x'(t) = x(t)e^{-i[\Phi(t)-\Phi_0]}, \quad (16)$$

giving a complex dataset in which the signal is given by $h'(t) = h(t)e^{-i[\Phi(t)-\Phi_0]}$. The now complex signal is

$$\begin{aligned} h'(t) = & h_0 \left(\frac{1}{4}F_+(1 + \cos^2\iota) \cos \Phi_0 + \frac{1}{2}F_\times \cos \iota \sin \Phi_0 \right) + \\ & ih_0 \left(\frac{1}{4}F_+(1 + \cos^2\iota) \sin \Phi_0 - \frac{1}{2}F_\times \cos \iota \cos \Phi_0 \right), \end{aligned} \quad (17)$$

where F_+ and F_\times are given by Eqs. 7 and 8. This heterodyne therefore removes the fast-varying part of the signal (the time dependent part of Eq. 9) leaving a complex data stream with the signal shifted to zero frequency (setting aside small offsets due to the diurnal amplitude modulation of the signal from the detector beam pattern). In practice this heterodyne is performed in a two stage process. First a *coarse* heterodyne is performed using the phase evolution calculated assuming a stationary frame. This data is then low-pass filtered (in this case using a 9th order Butterworth filter with a 0.25 Hz knee frequency) and heavily downsampled from the original rate of 16 384 Hz to 1 Hz. A second stage of heterodyne takes into account the signal's modulation due to the Earth's motion and relativistic effects (see Eq. 13). The data are then further downsampled from 1 Hz to 1/60 Hz by taking the mean of 60 samples, which has the effect of an additional low pass filter.

4.1.2. Data cleaning

The fully heterodyned data are cleaned to remove the largest outliers, by discarding points with absolute values greater than 5 times the standard deviation of the data. This cleaning is performed twice to combat the effect of extreme outliers (many order of magnitude larger than normal) skewing the standard deviation estimate. This removes $\sim 0.05\%$ of the data.

For the parameter estimation, as in (Abbott et al. 2007, 2010), the likelihood calculation assumes the data is stationary for contiguous 30 minute segments, although shorter segments of 5 minutes or more are also included to account for shorter stretches of data at the end of longer contiguous segments. This contiguity requirement removes a further $\sim 0.2\%$ of the heterodyned data, which is within segments shorter than 5 minutes.

4.1.3. Parameter estimation and upper limits

This new, and far smaller, 1/60 Hz-sampled dataset is then used to estimate the four unknown signal parameters h_0 , Φ_0 , $\cos \iota$, and ψ . These are estimated using a Bayesian formalism, with a Students- t -like distribution for the likelihood (formed by marginalizing a Gaussian likelihood over an unknown noise standard deviation) given the heterodyned data and a signal model from Eq. 17, and specific priors (see below) on these parameters. This posterior probability volume is explored using a Markov chain Monte Carlo (Abbott et al. 2010), which gives posterior probability distribution functions (PDFs) on each parameter marginalized over the three others.

In this analysis two different sets of independent priors are used for the parameters. In one case uniform priors on all four parameters are set – for the angular parameters this means that they are uniform across their allowable ranges, but for h_0 the lower bound is zero, and the upper bound is set at a level well above any values that could be consistent with the data. For reasons set out in Section 1 the other case sets the priors on ψ and $\cos \iota$ to be Gaussians given by Eq. 1, whilst keeping the h_0 and Φ_0 priors as uniform.

The marginalised h_0 posterior, $p(h_0|d, I)$, can be used to set an upper limit in the amplitude by finding the value of h_0^{ul} that bounds (from zero) the cumulative probability to a given degree-of-belief, B ,

$$B = \int_0^{h_0^{\text{ul}}} p(h_0|d, I)dh_0. \quad (18)$$

Here we set 95% degree-of-belief upper limits. Due to the fact that the MCMC is finite in length there will be small statistical uncertainties between different MCMC runs, which for cleaned data we find to be $\lesssim 1 \times 10^{-26}$. The difference in results between using cleaned and non-cleaned data, as above, is within the statistical uncertainty from the MCMC.

4.2. \mathcal{F} and \mathcal{G} statistics method

The second search method uses the \mathcal{F} and \mathcal{G} statistics developed in (Jaranowski et al. 1998) and (Jaranowski & Królak 2010). These statistics are used to perform maximum-likelihood estimation of signal parameters and to obtain frequentist upper limits on the signal amplitude.

4.2.1. Data reduction

The description of how to compute the \mathcal{F} and \mathcal{G} statistics from time-domain data is given in (Jaranowski et al. 1998) and (Jaranowski & Królak 2010). The \mathcal{F} statistic is applied when the four parameters h_0 , Φ_0 , ψ and ι are assumed to be unknown. When the orientation of the spin axis of the Vela pulsar and the wave polarization angle are known and given by Eqs. 1, the \mathcal{G} statistic is used instead.

We have refined the application of these statistics to account for two features of the current search. Firstly, the VSR2 data that we analyze are not stationary (see Figure 6), so the statistics must be adjusted to de-emphasize noisy periods. Secondly, we use as our input data the complex-valued *coarse* heterodyne data described in Section 4.1, so the statistics must be generalized to deal with complex data. These effects can be taken into account in \mathcal{F} and \mathcal{G} statistics formalism in a straightforward way derived explicitly in Appendix C, resulting in the generalized forms of the \mathcal{F} and \mathcal{G} statistics given by Eqs. C11 and C15, respectively. These generalized forms of the statistics are used to search VSR2 data for a gravitational wave signal from the Vela pulsar.

4.2.2. Data cleaning

The coarse heterodyne data that we analyze with the \mathcal{F} and \mathcal{G} statistics contains a small number of outliers that must be discarded. To identify these outliers we have used an iterative method called the Grubbs’ test (Grubbs 1969) explained in detail in Appendix D. Application of the Grubbs’ test resulted in removal of 0.1% of the total data points in input data, amounting to a negligible loss of signal-to-noise ratio of any continuous signal present in the data.

4.2.3. Parameter estimation and upper limits

In the frequentist approach, a signal is detected in the data if the value of the \mathcal{F} or \mathcal{G} statistic exceeds some threshold corresponding to an accepted false alarm probability (1% in this analysis). When the values of the statistics are not statistically significant, we can set upper limits on the amplitude h_0 of the GW signal. We choose a frequentist framework by computing the amplitude h_0^* of a signal that, if truly present in the data, would produce a value of the detection statistic that in 95% of the cases would be larger than the value actually found in the analysis. To obtain the upper limits on h_0 we follow a Monte Carlo method described in (Abbott et al. 2004). That is, we add simulated GW signals to the VSR2

data and determine the resulting values of the statistics. The parameters of the simulated signals are exactly the same as for Vela, except for the gravitational-wave frequency which is randomly offset from twice the Vela spin frequency. For the \mathcal{F} statistic case, the parameters ψ and $\cos\iota$ are chosen from a uniform distribution, whereas for \mathcal{G} statistic case they are fixed to the values estimated from X-ray observations (see Eq.1). We calculate the upper limits corresponding to the obtained values of the statistics by interpolating results of the simulation to find the h_0 value for which 95% of the signals have a louder \mathcal{F} - or \mathcal{G} -statistic value than that obtained in the search. To estimate the statistical errors in the upper limits from the Monte Carlo simulations we have followed the method presented in Section IVE of (Abbott et al. 2004) by performing an additional set of injections for the amplitude h_0 around the obtained upper limits.

In the case that a statistically significant signal is detected we can estimate unknown signal parameters. In the case of the \mathcal{F} statistic search the maximum likelihood estimators of the amplitudes are obtained by equations C12. These amplitude estimates are then transformed into estimates of parameters h_0 , Φ_0 , ψ and ι using Eqs. 23 of (Jaranowski & Królak 2010). In the case of the \mathcal{G} statistic search, where parameters ψ and ι are assumed to be known, the amplitude estimator is obtained by Eq. C17, and estimates of the parameters h_0 and Φ_0 are calculated from Eqs. 7 of (Jaranowski & Królak 2010).

4.3. Matched filter on the signal Fourier components

The third search method uses the Fourier amplitudes computed at five frequencies where the signal would appear due to sidereal amplitude modulation, and applies a matched filter to this 5-point complex data vector. Further details can be found in Appendix A and in (Astone et al. 2010).

4.3.1. Data reduction

The starting point for this method is a short Fourier transform database (SFDB) built from calibrated strain data sampled at 4096 Hz (Astone et al. 2005). The FFTs have a duration of 1024s and are interlaced by 50% and windowed with a flat top - cosine edges window. From the SFDB a small band (0.2 Hz in this analysis) around the frequency of interest is extracted from each FFT. The SFDB contains, among other information, the position and the velocity of the detector in the SSB at the center time of each FFT. Each frequency domain chunk is zero-padded and inversely Fourier-transformed to obtain a complex time series

with the same sampling time of the original time series, but with a spectrum different from zero only in the selected band (*i.e.*, it is an *analytical signal*, see *e.g.*, (Astone *et al.* 2002)). Then, for each sample, the detector position in the SSB is computed, by interpolating with a 3rd degree polynomial. The Doppler and Einstein effects can be seen as a varying time delay $\Delta(t)$. A new non-uniformly-sampled time variable t' with samples $t'_i = t_i + \Delta(t_i)$ is computed. The spin-down is corrected by multiplying each data chunk by $e^{-i\Delta\phi_{sd}(t')}$ where $\Delta\phi_{sd}(t') = 2\pi \left(\dot{f} \frac{t'^2}{2} + \ddot{f} \frac{t'^3}{6} \right)$. Then the data are resampled at equal intervals in t' . The final complex time series has a sampling frequency of 1Hz. At this point, a true GW signal would be sinusoidal with a sidereally-modulated amplitude and phase, as described in Sec.(2), containing power at the nominal source frequency and in lower and upper sidebands of $\pm\Omega_{\oplus}, \pm 2\Omega_{\oplus}$. The Fourier coefficients at these five frequencies are taken to form a complex data 5-vector \mathbf{X} .

The detection method described here relies on a description of the GW signal given in Appendix A. When the polarization angle ψ and the inclination angle of the star rotation axis ι are unknown, we use a procedure that we denote *four-degrees of freedom detection*, in which the two signal 5-vectors $\mathbf{A}^+, \mathbf{A}^\times$, corresponding to the + and \times polarizations and defined in Appendix A, are numerically computed and projected onto the data 5-vector \mathbf{X} :

$$\hat{H}_+ = \frac{\mathbf{X} \cdot \mathbf{A}^+}{|\mathbf{A}^+|^2} \quad (19)$$

$$\hat{H}_\times = \frac{\mathbf{X} \cdot \mathbf{A}^\times}{|\mathbf{A}^\times|^2}. \quad (20)$$

The output of the two matched filters are the estimators of the amplitudes $H_0 e^{i\Phi_0} H_+$, $H_0 e^{i\Phi_0} H_\times$. The final detection statistic is defined by

$$S = |\mathbf{A}^+|^4 |\hat{H}_+|^2 + |\mathbf{A}^\times|^4 |\hat{H}_\times|^2. \quad (21)$$

More details can be found in (Astone *et al.* 2010).

If estimations of ψ and ι provided by X-ray observations (Section 1) are used, we can apply a simpler procedure that we call a *two-degrees of freedom detection*. In this case the signal is completely known, apart from an overall complex amplitude $H = H_0 e^{i\Phi_0}$. Then, the template consists of just one 5-vector $\mathbf{A} = H_+ \mathbf{A}^+ + H_\times \mathbf{A}^\times$, where H_+, H_\times are given by Eqs. A3, and only one matched filter must be applied to the data 5-vector \mathbf{X} :

$$\hat{H} = \frac{\mathbf{X} \cdot \mathbf{A}}{|\mathbf{A}|^2}, \quad (22)$$

which provides an estimation of the signal complex amplitude. The detection statistic is then given by $S = |\hat{H}|^2$.

4.3.2. Data cleaning

In addition, various cleaning steps were applied to the data. The data can be modeled as a Gaussian process, with slowly varying variance, plus some unmodeled pulses affecting the tails of data distribution. The cleaning procedure consists of two parts. First, before the construction of the SFDB, high-frequency time domain events are identified after applying to the data a first-order Butterworth high-pass bilateral filter, with a cut-off frequency of 100 Hz. These events are then subtracted from the original time series. In this way we do not reduce the observation time because we are simply removing from the data the high-frequency noisy component. The effect of this kind of cleaning has been studied in data from Virgo Commissioning and Weekly Science runs and typically reduces the overall noise level by up to 10–15%, depending on the quality of the data (Acernese *et al.* 2009). After Doppler and spin-down correction, further outliers that appear in the small band to be analyzed are also removed from the dataset by using a threshold of $\pm 5 \times 10^{-21}$ on the data strain amplitude, reducing the amount of data by $\sim 1.3\%$. Slow non-stationarity of the noise is taken into account by applying a *Wiener* filter to the data, in which we estimate the variance of the Gaussian process over periods of ~ 1000 s, and weight the data with its inverse in order to de-emphasize the more disturbed periods.

4.3.3. Parameter estimation and upper limits

Following the frequentist prescription, the value of S obtained from the search is compared with a threshold S^* corresponding to a given false alarm probability (1% in this analysis). If $S > S^*$, then one has a potential signal detection deserving deeper study. In the case of signal detection, the signal parameters can be estimated from \hat{H}_+ , \hat{H}_\times , using the relations shown in Appendix B. If the measured S value lies below the threshold, we can set an upper limit on the amplitude of a possible signal present.

The determination of upper limits is carried out via Monte Carlo simulations similar to the limit determination described in Section 4.2.3. In the case of 4 degrees of freedom (*d.o.f.*), the unknown parameters, ψ and $\cos \iota$ were taken to be uniformly distributed. The analysis method allows us to establish an upper limit for the wave amplitude H_0 defined in Appendix A. This was translated into an upper limit on h_0 , under the assumption that the source is a tri-axial neutron star, using Eq. A5 after maximising the factor under the square root with respect to the inclination angle. In this way the upper limit we obtain is conservative. In the 2 *d.o.f.* case we compute the upper limit by using for ψ and ι the values given in Eqs. 1.

The statistical error associated with the Monte Carlo simulations is estimated as half of the difference between the two signal amplitudes that bound the 95% confidence level. The grid in the amplitude of the injected signals has been chosen fine enough that the resulting statistical error is about one order of magnitude smaller than the systematic error coming from calibration and actuation uncertainty.

5. Results from the searches

In the analyses all available science mode data recorded by Virgo were used. No evidence for a continuous gravitational wave signal was seen using any of the three analysis methods described in Section 4. We have therefore used the data to set upper limits on the gravitational wave amplitude.

For the *complex heterodyne* method (Section 4.1) the marginalised posteriors for the four parameters, using the two different priors, are shown in Figs. 4 and 5. The presence of a detectable signal would show up as a posterior distribution in h_0 that is peaked away from $h_0 = 0$. The observed distributions are consistent with no signal being present. The 95% credible limits on h_0 are shown and have values 2.4×10^{-24} and 2.1×10^{-24} respectively (note that the strongly-peaked distributions for $\cos \iota$ and ψ in Fig. 4 are simply the restricted priors placed on those parameters).

For the \mathcal{F} and \mathcal{G} statistics (Section 4.2), the values obtained were consistent with false alarm probabilities of 22% and 35%, respectively. Since these probabilities are far above our 1% false alarm threshold, we conclude that the data are consistent with the absence of a signal. Using the Monte Carlo method described in Sec. 4.2.3, we set 95% confidence upper limits on h_0 of 2.4×10^{-24} and 2.2×10^{-24} , respectively.

For the matched filter on Fourier components (Section 4.3), the values computed for the *4 d.o.f* and *2 d.o.f* statistics were consistent with false alarm probabilities of 46% and 40%, respectively. Again we conclude that the data are consistent with the absence of a signal. We obtain 95% confidence upper limits on h_0 of 2.2×10^{-24} and 1.9×10^{-24} , respectively.

The results for all three analyses are summarized in Table 3, which also includes the systematic uncertainty in the upper limit from calibration and actuation uncertainties. For each analysis, results are given both for the case in which ψ and $\cos \iota$ are assumed to be known (*i.e.* with restricted priors) and unknown (*i.e.* with unrestricted priors).

We emphasize once again that the two results for the complex heterodyne method are Bayesian 95% credible limits on h_0 , while the \mathcal{G} , \mathcal{F} , *2 d.o.f*, and *4 d.o.f* results are frequentist

95% confidence upper limits. While we would expect the two types of upper limit to be *similar* in value, they are not directly comparable, because they address different questions. The Bayesian question asks: “Given our priors and our data, for what value of h_0 are we 95% certain that any true signal lies below that value?” The frequentist question asks: “Above what value of h_0 would a signal produce a larger value of our statistic 95% of the time?” The subtle difference between these questions means that they may give different answers for the same data, and we should not read too much into the fact that in *this* search the two approaches gave very similar numbers.

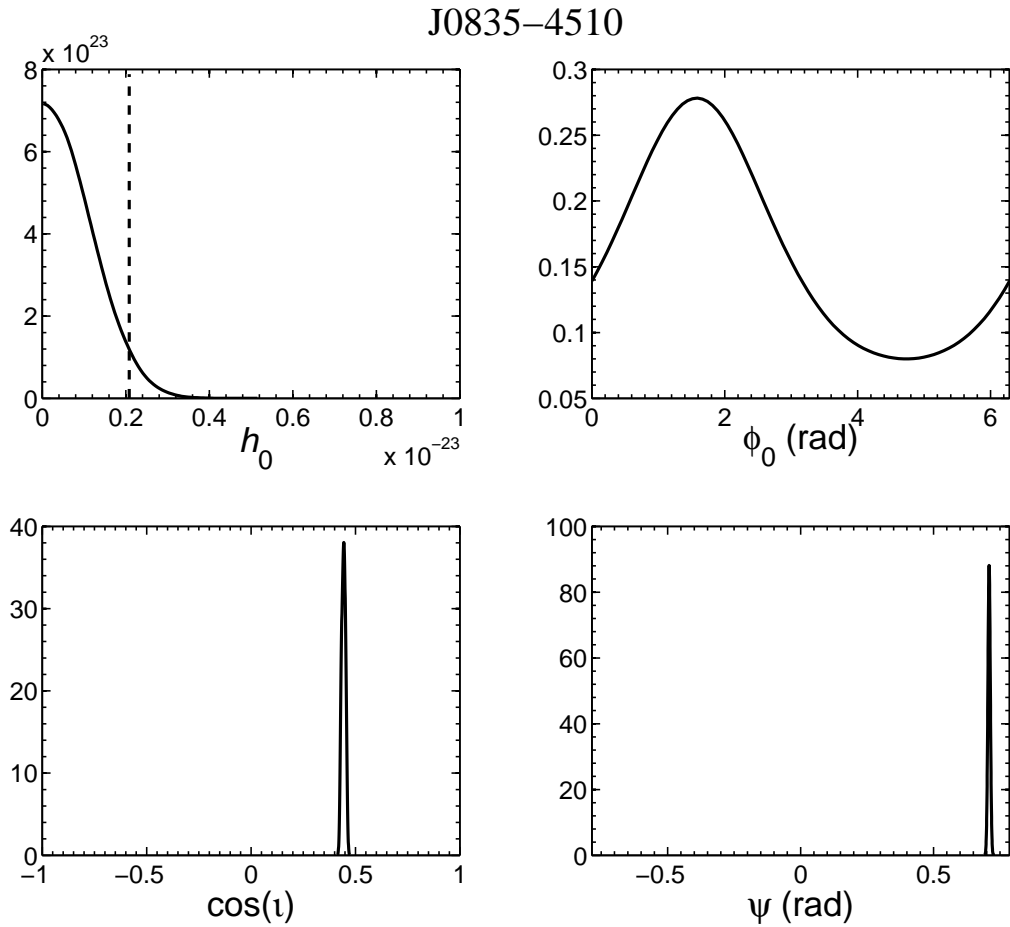


Fig. 4.— The posterior PDFs for the pulsar parameters h_0 , Φ_0 , $\cos \iota$ and ψ for PSR J0835–4510, produced using restricted priors on $\cos \iota$ and ψ with the complex heterodyne method. The vertical dashed line shows the 95% upper limit on h_0 .

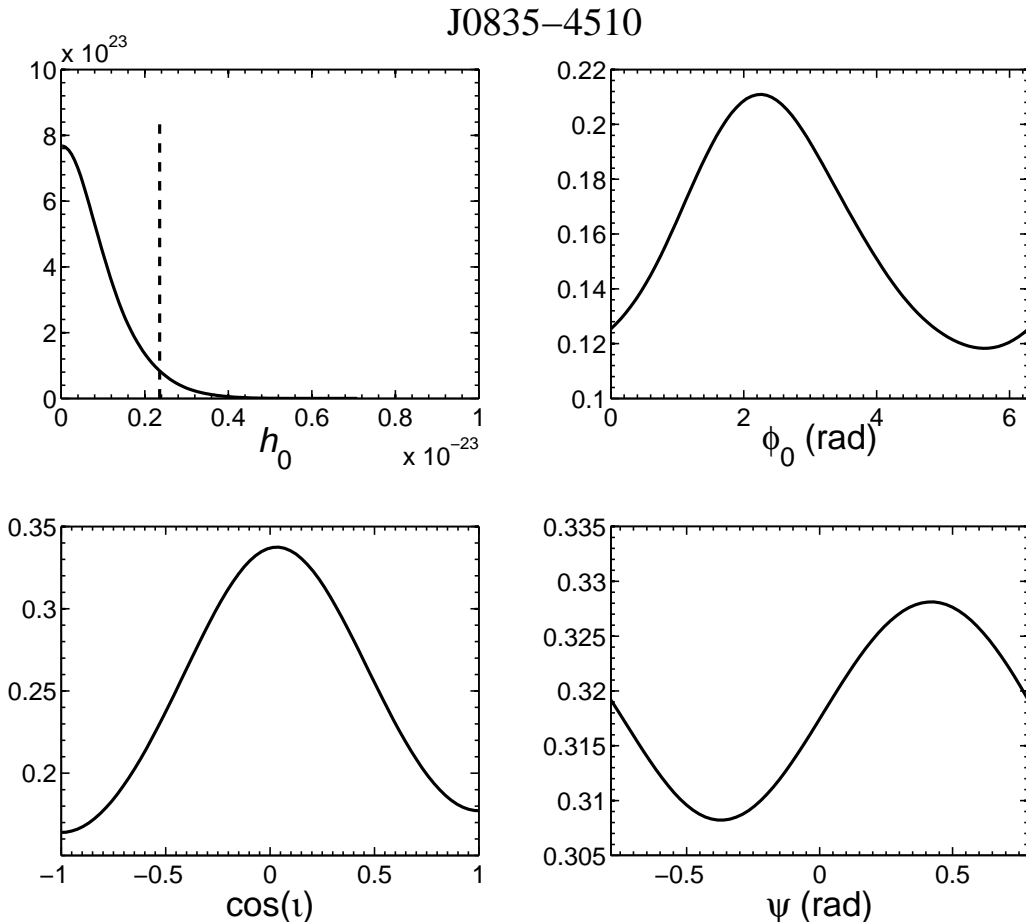


Fig. 5.— The posterior PDFs for the pulsar parameters h_0 , Φ_0 , $\cos i$ and ψ for PSR J0835–4510, produced using uniform priors for $\cos i$ and ψ across the range of their possible values with the complex heterodyne method. The vertical dashed line shows the 95% upper limit on h_0 .

5.1. Validation with hardware injections

All three pipelines used in the analysis have been tested with both software and hardware injections of CW signals in the VSR2 data. In particular we discuss here hardware injections. For the entire duration of the run 13 CW signals (named *Pulsar0-12*) have been injected in the Virgo detector by sending the appropriate excitations to the coils used to control one mirror’s position. These signals were characterized by various amplitudes, spanned a frequency range from ~ 20 Hz to ~ 1400 Hz, and covered a range of values for the spin-down \dot{f} from $\sim -4 \times 10^{-18}$ Hz s $^{-1}$ to $\sim -2.5 \times 10^{-8}$ Hz s $^{-1}$. The corresponding source position (α, δ) ,

inclination ι of the source spin axis, and polarization angle ψ were chosen randomly. All the injected signals have been generated using the same software as the signals injected in LIGO S5 and previous runs. Injected signals *Pulsar0-9* have also the same parameters as the LIGO injections, while *Pulsar10-12* have very low frequency and have been injected in Virgo only. The three pipelines were exercised on several of these simulated signals. The pipelines have been able to detect the signals and to estimate their parameters with good accuracy when the signal-to-noise ratio (SNR) is sufficient. In particular, in Tables 5-7 we report the results obtained for *Pulsar3*, characterized by a very small spin-down and high SNR, *Pulsar5* with low frequency, very small spin-down and relatively low SNR and *Pulsar8* with high spin-down and SNR. The frequency parameters for these three injections are given in Table 4. There is good agreement between the true and recovered signal parameters. With the method based on matched filtering on the signal Fourier components the estimation of the signal absolute phase is not straightforward.

6. Conclusions

In this paper we present the results of the analysis of Virgo VSR2 run data for the search of continuous GW signals from the Vela pulsar. The data have been analyzed using three largely independent methods and assuming that the gravitational wave emission follows the radio timing. For an assumed known orientation of the star’s spin axis and value of the polarization angle, two methods have determined frequentist upper limits at 95% confidence level of, respectively, 1.9×10^{-24} and 2.2×10^{-24} . The third method has determined a Bayesian 95% degree-of-belief upper limit of 2.1×10^{-24} . The lowest of these is about 41% below the indirect spin-down limit. It corresponds to a limit on the star ellipticity of 1.1×10^{-3} , which is well above the maximum equatorial ellipticity that a neutron star with a ‘standard’ equation of state can sustain, but comparable to the maximum value permitted by some exotic equations of state (Owen 2005; Lin 2007; Haskell et al. 2007). Given that the power emitted in GW is $\dot{E}_{GW} = -\frac{32\pi^6 G}{5c^5} I_{zz}^2 \epsilon^2 f^6$, our results constrain the fraction of spin-down energy due to the emission of GW to be below 35%. For an unknown orientation of the star’s spin axis and polarization angle the two frequentist upper limits are, respectively, 2.2×10^{-24} and 2.4×10^{-24} while the Bayesian upper limit is 2.4×10^{-24} . The lowest of these is about 33% below the spin-down limit. In this case the limit on the star ellipticity is 1.2×10^{-3} , while the corresponding limit on the fraction of spin-down energy emitted through GW is 45%. These numbers assume the canonical value for the star moment of inertia, $I = 10^{38} \text{ kg m}^2$. However, the theoretically predicted values of I vary in the range $\sim 1 - 3 \times 10^{38} \text{ kg m}^2$ (Abbott et al. 2010), so our upper limit on the ellipticity can be considered as conservative. Such ellipticities could also be sustained by internal toroidal magnetic fields of order 10^{16} G ,

Table 3. Estimated 95% upper limit on h_0 for PSR J0835–4510 from the three different analysis methods (the horizontal line separates Bayesian from frequentist results). The systematic error on amplitude from calibration and actuation amounts to $\sim 5.5\%$, as discussed in Section 3. This corresponds to an uncertainty on the upper limits of about $\pm 0.1 \times 10^{-24}$. For all upper limits the statistical error, associated with the Monte Carlo simulations used to establish the limit itself, is about one order of magnitude smaller.

Analysis method	95% upper limit for h_0
Heterodyne, restricted priors	$(2.1 \pm 0.1) \times 10^{-24}$
Heterodyne, unrestricted priors	$(2.4 \pm 0.1) \times 10^{-24}$
\mathcal{G} -statistic	$(2.2 \pm 0.1) \times 10^{-24}$
\mathcal{F} -statistic	$(2.4 \pm 0.1) \times 10^{-24}$
MF on signal Fourier components, 2 d.o.f.	$(1.9 \pm 0.1) \times 10^{-24}$
MF on signal Fourier components, 4 d.o.f.	$(2.2 \pm 0.1) \times 10^{-24}$

Table 4. Frequency and positional parameters for the hardware injections ($\ddot{f} = 0$ for all the injections). The reference time epoch for the source frequency is MJD=52944 for all the injections. The optimal signal-to-noise ratio (SNR) is also given.

Name	f [Hz]	\dot{f} [Hz s $^{-1}$]	α [deg]	δ [deg]	SNR
<i>Pulsar3</i>	108.8571594	-1.46×10^{-17}	178.372574	-33.436602	192
<i>Pulsar5</i>	52.80832436	-4.03×10^{-18}	302.626641	-83.8391399	40
<i>Pulsar8</i>	194.3083185	-8.65×10^{-9}	351.389582	-33.4185168	197

Table 5. Estimated parameters for hardware injection *Pulsar3* from the three different analysis methods.

Method	$\frac{h_{0,found}}{h_{0,inj}}$	ι [$\iota_{inj} = 1.651$]	ψ [$\psi_{inj} = 0.444$]	Φ_0 [$\Phi_{0,inj} = 5.53$]
Heterodyne	0.97	1.67	0.43	5.55
\mathcal{F} -statistic	0.96	1.65	0.44	5.54
MF on signal Fourier comp., 4 d.o.f.	0.96	1.66	0.44	*

depending on the field configuration, equation of state, and superconductivity of the star (Akgun & Wassermann 2007; Haskell et al. 2008; Colaiuda et al. 2008; Ciolfi et al. 2010). Then, our results have constrained the internal toroidal magnetic field of the Vela to be less than of the order of that value (it must be stressed, however, that the stability of a star with an internal field much larger than the external one is still an open issue). Vela is the second young pulsar for which the spin-down limit has now been beaten.

A more stringent constraint on the emission of GW from the Vela pulsar may be established by analyzing data of the next Virgo+ run (VSR4) which is tentatively scheduled for summer 2011 and should last a few months. This run, assuming the planned sensitivity is reached, could be able to probe values of the Vela pulsar ellipticity below a few units in 10^{-4} , corresponding to a fraction of spin-down energy emitted through the emission of GW below a few percent. We note that this run will also provide interesting results for several other low frequency pulsars. In particular, it could allow detection of GW from the Crab pulsar and J1952+3252 if their ellipticities are larger than $\sim 10^{-5}$, a value nearly compatible with the maximum deformation allowed by standard neutron star equations of state.

Second-generation detectors are expected to have a still better sensitivity at low frequency. Advanced Virgo (Acernese et al. 2009) and Advanced LIGO (Harry & the LIGO Scientific Collaboration 2010), which should enter into operation around 2014–2015, in one year could detect a GW signal from the Vela pulsar if its ellipticity is larger than a few times 10^{-5} , the corresponding fraction of spin-down energy emitted through GW being below a few times 10^{-4} in this case.

The possibility of building a third generation GW detector, with a sensitivity a factor of 10 or more better than Advanced detectors in a wide frequency range, is also being studied. The Einstein Telescope (Punturo et al. 2010), which is currently at the stage of design study, is expected to release its first science data around 2025–2027. It should be able to detect GWs from the Vela pulsar, using one year of data, for ellipticity larger than $4 \times 10^{-7} - 10^{-6}$, depending on the detector configuration that will be chosen.

Table 6. Estimated parameters for hardware injection *Pulsar5* from the three different analysis methods.

Method	$\frac{h_{0,found}}{h_{0,inj}}$	ι (η) [$\iota_{inj} = 1.089$]	ψ [$\psi_{inj} = -0.364$]	Φ_0 [$\Phi_{0,inj} = 2.23$]
Heterodyne	0.90	0.99	−0.27	2.05
\mathcal{F} -statistic	0.89	0.98	−0.27	2.10
MF on signal Fourier comp., 4 d.o.f.	0.97	0.96	−0.26	*

We dedicate this paper to the memory of our friend and colleague Stefano Braccini, who made very important contributions to the development of the Virgo detector and, more recently, contributed to the search effort for CW signals with his usual enthusiasm and skilfulness.

The authors gratefully acknowledge the support of the United States National Science Foundation for the construction and operation of the LIGO Laboratory, the Science and Technology Facilities Council of the United Kingdom, the Max-Planck-Society, and the State of Niedersachsen/Germany for support of the construction and operation of the GEO600 detector, and the Italian Istituto Nazionale di Fisica Nucleare and the French Centre National de la Recherche Scientifique for the construction and operation of the Virgo detector. The authors also gratefully acknowledge the support of the research by these agencies and by the Australian Research Council, the Council of Scientific and Industrial Research of India, the Istituto Nazionale di Fisica Nucleare of Italy, the Spanish Ministerio de Educación y Ciencia, the Conselleria d’Economia Hisenda i Innovació of the Govern de les Illes Balears, the Foundation for Fundamental Research on Matter supported by the Netherlands Organisation for Scientific Research, the Polish Ministry of Science and Higher Education, the FOCUS Programme of Foundation for Polish Science, the Royal Society, the Scottish Funding Council, the Scottish Universities Physics Alliance, The National Aeronautics and Space Administration, the Carnegie Trust, the Leverhulme Trust, the David and Lucile Packard Foundation, the Research Corporation, and the Alfred P. Sloan Foundation.

A. An alternative formalism to describe a continuous GW signal

The continuous GW signal emitted by a *generic* rotating rigid star can be described by a polarization ellipse. The polarization ellipse is characterized by the ratio $\eta = \frac{a}{b}$ of its semi-minor to its semi-major axis and by the angle ψ defining the direction of the major axis. The angle ψ is the same introduced in Sec. 2. The ratio η varies in the range $[-1, 1]$,

Table 7. Estimated parameters for hardware injection *Pulsar8* from the three different analysis methods.

Method	$\frac{h_{0,found}}{h_{0,inj}}$	ι (η) [$\iota_{inj} = 1.497$]	ψ [$\psi_{inj} = 0.170$]	Φ_0 [$\Phi_{0,inj} = 5.89$]
Heterodyne	0.97	1.49	0.18	5.90
\mathcal{F} -statistic	0.95	1.49	0.17	6.07
MF on signal Fourier comp., 4 d.o.f.	0.98	1.50	0.17	*

where $\eta = 0$ for a linearly polarized wave and $\eta = \pm 1$ for a circularly polarized wave. The (complex) signal can be expressed as

$$\mathbf{h}(t) = H_0 (H_+ \mathbf{e}_+ + H_\times \mathbf{e}_\times) e^{i\Phi(t)}, \quad (\text{A1})$$

where \mathbf{e}_+ and \mathbf{e}_\times are the two polarization tensors and the *plus* and *cross* amplitudes are given by

$$H_+ = \frac{\cos 2\psi - i\eta \sin 2\psi}{\sqrt{1 + \eta^2}} \quad (\text{A2})$$

$$H_\times = \frac{\sin 2\psi + i\eta \cos 2\psi}{\sqrt{1 + \eta^2}}. \quad (\text{A3})$$

If we consider, as in Section 2, a triaxial neutron star rotating around a principal axis of inertia the following relations among H_0, η and h_0, ι hold:

$$\eta = -\frac{2 \cos \iota}{1 + \cos^2 \iota} \quad (\text{A4})$$

$$H_0 = \frac{h_0}{2} \sqrt{1 + 6 \cos^2 \iota + \cos^4 \iota}. \quad (\text{A5})$$

In terms of $+$ and \times components we have

$$H_{+, \psi=0} = \frac{h_+}{H_0} = h_0 \frac{(1 + \cos^2 \iota)}{2H_0} \quad (\text{A6})$$

$$\Im(H_{\times, \psi=0}) = -\frac{h_\times}{H_0} = -\frac{h_0 \cos \iota}{H_0}. \quad (\text{A7})$$

In this formalism the complex gravitational strain at the detector is given by

$$h(t) = H_0 (A_+(t)H_+ + A_\times(t)H_\times) e^{i\Phi(t)}, \quad (\text{A8})$$

where

$$A_+ = F_+(\psi = 0) \quad (\text{A9})$$

$$A_\times = F_\times(\psi = 0). \quad (\text{A10})$$

After Doppler and spin-down corrections, as described in Sec. 4.3, we have:

$$h(t) = H_0 (A_+(t)H_+ + A_\times(t)H_\times) e^{i(\omega_0 t + \Phi_0)}. \quad (\text{A11})$$

We now introduce the *signal 5-vectors* for the $+$ and \times components, \mathbf{A}^+ , \mathbf{A}^\times , given by the Fourier components, at the 5 frequencies produced by the amplitude and phase modulation, of the detector response functions A_+ , A_\times . It is straightforward to see that the signal in the antenna is completely defined by the 5-components complex vector

$$\mathbf{A} = H_0 e^{i\Phi_0} (H_+ \mathbf{A}^+ + H_\times \mathbf{A}^\times). \quad (\text{A12})$$

More details can be found in (Astone et al. 2010).

B. Parameter estimators for MF on signal Fourier components

Once the two estimators \hat{H}_+ , \hat{H}_\times have been computed from the data, if a detection is claimed, the signal parameters H_0 , η , ψ can be estimated using the following relations. The estimator of the signal amplitude is given by

$$\hat{H}_0 = \sqrt{|\hat{H}_+|^2 + |\hat{H}_\times|^2}. \quad (\text{B1})$$

Introducing the quantities

$$\hat{H}_+ \cdot \hat{H}_\times = A + iB, \quad (\text{B2})$$

$$|\hat{H}_+|^2 - |\hat{H}_\times|^2 = C, \quad (\text{B3})$$

where the scalar product is between two complex numbers and includes a complex conjugation of one, the estimation of the ratio between the axes of the polarization ellipse is

$$\hat{\eta} = \frac{-1 + \sqrt{1 - 4B^2}}{2B}, \quad (\text{B4})$$

while the estimation of the polarization angle can be obtained from

$$\cos(4\hat{\psi}) = \frac{C}{\sqrt{4A^2 + B^2}} \quad (\text{B5})$$

$$\sin(4\hat{\psi}) = \frac{2A}{\sqrt{4A^2 + B^2}}. \quad (\text{B6})$$

C. \mathcal{F} and \mathcal{G} statistics for complex heterodyne data in non-stationary, uncorrelated noise

We assume that the noise in the data is Gaussian and uncorrelated. In order to take into account non-stationarity of the data, we assume that each noise sample $n(l)$ in the data time series is drawn from a Gaussian distribution with a variance $\sigma^2(l)$. We assume that the Gaussian distributions in question have zero means. Thus the autocorrelation function $K(l, l')$ for the noise is given by

$$K(l, l') = \sigma^2(l) \delta_{ll'}, \quad (\text{C1})$$

where l, l' are integers and where $\delta_{ll'}$ is Kronecker's delta function. Let us first assume that the signal $h(l)$ is completely known and that the noise is additive. Thus when the signal is present the data take the following form

$$x(l) = n(l) + h(l). \quad (\text{C2})$$

For Gaussian noise the optimal filter $q(l)$ is the solution of the following (integral) equation (see (Jaranowski & Królak 2009), p. 72)

$$h(l) = \sum_{l'=1}^N K(l, l')q(l'), \quad (\text{C3})$$

where N is the number of data points. Consequently we have the following equation for the filter $q(l)$

$$q(l) = \frac{h(l)}{\sigma^2(l)} \quad (\text{C4})$$

and the following expression for the log likelihood ratio $\ln \Lambda$

$$\ln \Lambda[x] = \langle hx \rangle - \frac{1}{2} \langle h^2 \rangle, \quad (\text{C5})$$

where the operator $\langle \cdot \rangle$ is defined as

$$\langle gf \rangle = \sum_{l=1}^N \frac{g(l)f(l)}{\sigma^2(l)}. \quad (\text{C6})$$

Thus we see that for non-stationary Gaussian noise with the autocorrelation function (C1) the optimal processing is identical to matched filtering for a known signal in stationary Gaussian noise, except that we divide both the data and the filter by time-varying standard deviation of the noise. This may be thought as a special case of whitening the data and then correlating it using a whitened filter. The method is essentially the same as the Wiener filter introduced in Section 4.3. The generalization to the case of signal with unknown parameters is immediate.

In the analysis we use complex heterodyne data x_{het} ,

$$x_{het}(l) = x(l)e^{-i\Phi_{het}(l)}, \quad (\text{C7})$$

where Φ_{het} is the heterodyne phase (Φ_{het} can be an arbitrary real function). Thus we rewrite the \mathcal{F} and \mathcal{G} statistics and amplitude parameter estimators using complex quantities. We introduce complex amplitudes A_a and A_b

$$A_a = A_1 + iA_3, \quad (\text{C8})$$

$$A_b = A_2 + iA_4, \quad (\text{C9})$$

where the amplitudes A_k , $k = 1, 2, 3, 4$ are defined by Eqs. 23 of (Jaranowski & Królak 2010) and we also introduce the complex filters

$$\begin{aligned} h_a(l) &= a(l)e^{-i[\Phi(l)-\Phi_{het}(l)]} \\ h_b(l) &= b(l)e^{-i[\Phi(l)-\Phi_{het}(l)]}, \end{aligned} \quad (\text{C10})$$

where a and b are amplitude modulation functions (see Eqs. 7 and 8) defined by Eqs. 12 and 13 in (Jaranowski et al. 1998), and $\Phi(l)$ is the phase defined by Eq. 9.

The \mathcal{F} -statistic takes the following form

$$\mathcal{F} = \frac{\langle b^2 \rangle |\langle x_{het} h_a \rangle|^2 + \langle a^2 \rangle |\langle x_{het} h_b \rangle|^2 - 2 \langle a b \rangle \Re(\langle x_{het} h_a \rangle \langle x_{het} h_b \rangle^*)}{\langle a^2 \rangle \langle b^2 \rangle - \langle a b \rangle^2}, \quad (\text{C11})$$

and the complex amplitude parameter estimators are given by

$$\begin{aligned} \hat{A}_a &= 2 \frac{\langle b^2 \rangle \langle x_{het} h_a \rangle^* - \langle a b \rangle \langle x_{het} h_b \rangle^*}{\langle a^2 \rangle \langle b^2 \rangle - \langle a b \rangle^2}, \\ \hat{A}_b &= 2 \frac{\langle a^2 \rangle \langle x_{het} h_b \rangle^* - \langle a b \rangle \langle x_{het} h_a \rangle^*}{\langle a^2 \rangle \langle b^2 \rangle - \langle a b \rangle^2}. \end{aligned} \quad (\text{C12})$$

In the case of the \mathcal{G} -statistic it is useful to introduce a complex amplitude A

$$A = A_c + iA_s, \quad (\text{C13})$$

where real amplitudes A_c and A_s are defined by Eqs. 20 of (Jaranowski & Królak 2010) and a complex filter h_g

$$h_g = (h_c + ih_s)e^{i\Phi_{het}}, \quad (\text{C14})$$

where real filters h_c and h_s are defined by Eqs. 7 of (Jaranowski & Królak 2010). In complex notation the \mathcal{G} -statistic assumes the following simple form (cf Eq. 18 of (Jaranowski & Królak 2010))

$$\mathcal{G} = \frac{|\langle x_{het} h_g \rangle|^2}{2D}, \quad (\text{C15})$$

where

$$D = \langle |h_g|^2 \rangle. \quad (\text{C16})$$

The estimator of the complex amplitude A is given by

$$\hat{A} = \frac{\langle x_{het} h_g \rangle}{D}. \quad (\text{C17})$$

D. Grubbs' Test

The Grubbs' test (Grubbs 1969) is used to detect outliers in a univariate dataset. Grubbs' test detects one outlier at a time. This outlier is removed from the dataset and the test is iterated until no outliers are detected.

Grubbs' test is a test of the null hypothesis:

H0: *There are no outliers in the dataset x_i .*

against the alternate hypotheses:

H1: *There is at least one outlier in the dataset x_i .*

Grubbs’ test assumes that the data can be reasonably approximated by a normal distribution.

The Grubbs test statistic is the largest absolute deviation from the sample mean in units of the sample standard deviation and it is defined as:

$$G = \frac{\max |x_i - \mu|}{\sigma} \quad (\text{D1})$$

where μ and σ denote the sample mean and standard deviation, respectively.

The hypothesis of no outliers is rejected if

$$G > \frac{n-1}{\sqrt{n}} \sqrt{\frac{t_{\alpha/(2n),n-2}^2}{n-2+t_{\alpha/(2n),n-2}^2}}, \quad (\text{D2})$$

with $t_{\alpha/(2n),n-2}$ denoting the critical value of the t-distribution with $n-2$ degrees of freedom and a significance level of $\alpha/(2n)$.

We have applied the Grubbs’ test to the coarse heterodyne data before analyzing them with \mathcal{F} and \mathcal{G} statistics. We have applied the test to segments of 2^{16} data points and we have assumed false alarm probability of 0.1%. This resulted in identification of 13 844 outliers from the original dataset containing 12 403 138 points. We replaced these outliers with zeros. The time series before and after the removal of the outliers are presented in Fig. 6. The number of outliers constitutes 0.1% of the total data points in input data resulting in a negligible loss of signal-to-noise ratio of any continuous signal present in the data. With different methods to identify the outliers used by other searches the number of outliers was similar.

REFERENCES

- Abadie et al., J. 2010, ApJ, 722, 1504
 Abbott et al., B. 2004, Phys. Rev. D, 69, 082004

Coarse heterodyne VSR2 data from : 07-Jul-2009 21:00:00.500000 to: 08-Jan-2010 22:00:00.500000)

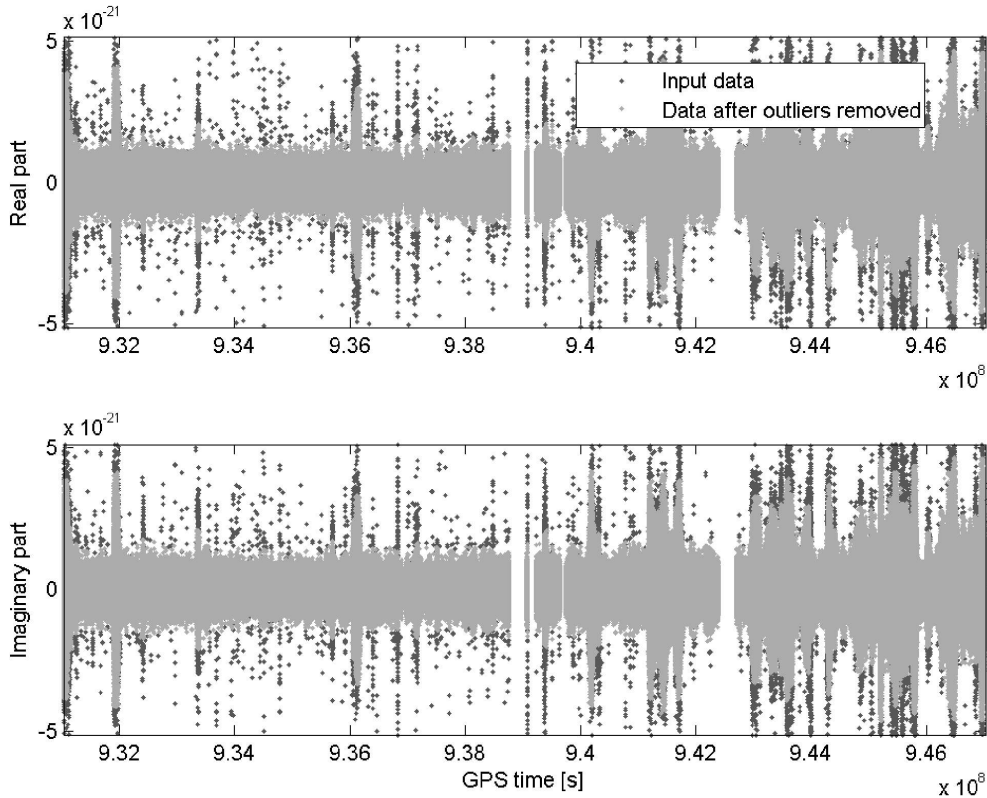


Fig. 6.— The coarse heterodyne data before (blue) and after (red) removal of the outliers using the Grubbs test. The top panel presents the real part of the data and the bottom panel the imaginary one. Not all the input data are shown because some outliers are large. There are 2814 and 2765 outliers outside the range of the plots for real and imaginary part of the data respectively.

—. 2007, *Phys. Rev. D*, 76, 042001

—. 2008, *ApJ*, 683, L45

—. 2010, *ApJ*, 713, 671

Accadia *et al.* 2010, *Classical and Quantum Gravity*, 28, 025005

Acernese *et al.*, F. 2009, VIR-027A-09, <https://tds.ego-gw.it/ql/?c=6589>

—. 2010, *Astroparticle Physics*, 33, 182

Acernese *et al.* 2009, *Classical and Quantum Gravity*, 20, 204002

- Akgun, T. & Wassermann, I. 2007, *MNRAS*, 383, 1551
- Akutsu et al., T. 2008, *Classical and Quantum Gravity*, 25, 184013
- Astone, P., D’Antonio, S., Frasca, S., & Palomba, C. 2010, *Classical and Quantum Gravity*, 27, 194016
- Astone, P., Frasca, S., & Palomba, C. 2005, *Classical and Quantum Gravity*, 22, S1197
- Astone *et al.* 2002, *Phys. Rev. D*, 65, 022001
- Buchner, S. 2010, *The Astronomer’s Telegram*, 2768
- Caraveo, P. A. & Bignami, G. F. 1989, *Space Science Reviews*, 49, 41
- Ciolfi, R., Ferrari, V., & Gualtieri. 2010, *MNRAS*, 406, 2540
- Colaiuda, A., Ferrari, V., Gualtieri, L., & Pons, J. 2008, *MNRAS*, 385, 2080
- Dodson, R., Legge, D., Reynolds, J. E., & McCulloch, P. M. 2003, *The Astrophysical Journal*, 596, 1137
- Dupuis, R. J. & Woan, G. 2005, *Phys. Rev. D*, 72, 102002
- Edwards, R. T., Hobbs, G. B., & Manchester, R. N. 2006, *MNRAS*, 372, 1549
- Grubbs, P. E. 1969, *Technometrics*, 11, 1
- Harry, G. M. & the LIGO Scientific Collaboration. 2010, *Classical and Quantum Gravity*, 27, 084006
- Haskell, B., Andersson, N., Jones, D. I., & Samuelsson, L. 2007, *Phys. Rev. Lett.*, 99, 231101
- Haskell, B., Samuelsson, L., Glampedakis, K., & Andersson, N. 2008, *MNRAS*, 385, 531
- Hobbs, G. B., Edwards, R. T., & Manchester, R. N. 2006, *MNRAS*, 369, 655
- Horowitz, C. J. & Kadau, K. 2009, *Phys. Rev. Lett.*, 102, 191102
- Jaranowski, P. & Królak, A. 2009, *Analysis of Gravitational-Wave Data* (Cambridge: Cambridge University Press)
- . 2010, *Classical and Quantum Gravity*, 27, 194015
- Jaranowski, P., Królak, A., & Schutz, B. F. 1998, *Phys. Rev. D*, 58, 063001

- Large, M. I., Vaughan, A. E., & Mills, B. Y. 1968, *Nature*, 220, 5165
- Lin, L.-M. 2007, *Phys. Rev. D*, 76, 081502
- Lyne, A. G. & Graham-Smith, F. 1998, *Pulsar Astronomy*, 2nd edn., Cambridge Astrophysics Series (Cambridge University Press)
- Lyne et al, A. G. 1996, *Nature*, 381, 497
- Misner, C., Thorne, K., & J.A., W. 1973, *Gravitation* (Freeman and Company)
- Ng, C.-Y. & Romani, W. 2008, *ApJ*, 673, 411
- Owen, B. 2005, *Phys. Rev. Lett.*, 95, 211101
- Palomba, C. 2000, *Astronomy & Astrophysics*, 354, 163
- Prix, R. & Krishnan, B. 2009, *Classical and Quantum Gravity*, 26, 204013
- Punturo et al., M. 2010, *Classical and Quantum Gravity*, 27, 194002